The Thesis Committee for Ugur Arslan
Certifies that this is the approved version of the following Thesis:

Limits and Ability of the Multichannel Analysis of Surface Waves Method to Detect and Resolve Subsurface Anomalies

APPROVED BY
SUPERVISING COMMITTEE:

Krishna Kumar, Supervisor

Brady R. Cox, Co-Supervisor

Limits and Ability of the Multichannel Analysis of Surface Waves Method to Detect and Resolve Subsurface Anomalies

by

Ugur Arslan

Thesis

Presented to the Faculty of the Graduate School of

The University of Texas at Austin

in Partial Fulfillment

of the Requirements

for the Degree of

Master of Science in Engineering

The University of Texas at Austin

December 2020

Dedication

To my parents, Gulsen Arslan and Mehmet Arslan, my brother, Onur Arslan, and my nephew, Murat Arslan.

Acknowledgements

I would like to thank the Republic of the Turkey and the General Directorate of State Hydraulic Works for the support that makes my education at the University of Texas at Austin possible.

I am extremely grateful to my co-supervisor, Dr. Brady Cox, who is one of the greatest mentors I have ever met. His kindness and guidance helped me to be a better version of myself. I would also like to show my gratitude to my supervisor, Dr. Krishna Kumar, who is a very dependable and hard-working person.

My sincere thanks to my undergraduate advisor, Dr. Ayhan Gurbuz, for always mentoring and supporting me.

I would also like to thank Joseph Vantassel for being available all the time whenever I needed help. He was a great friend and a mentor. I wish him the best on the road of becoming a professor.

Thank you to the friends who made my two-year experience at UT-Austin unforgettable.

Abstract

Limits and Ability of the Multichannel Analysis of Surface Waves Method to Detect and Resolve Subsurface Anomalies

Ugur Arslan, M.S.E

The University of Texas at Austin, 2020

Supervisor: Krishna Kumar

The multichannel analysis of surface waves (MASW) method is a non-invasive surface wave method used to characterize the layering and stiffness of the subsurface. This study assesses the practical limitations of using the MASW method for detecting and resolving subsurface anomalies. The sensitivity of MASW dispersion data to the presence of subsurface anomalies is examined through various two-dimensional (plane-strain) finite-difference elastic wave-propagation simulations. These simulations were performed on models containing anomalies of varying size, stiffness, and depth. The misfit between the dispersion data from a model with an anomaly (treatment model) and the same model without an anomaly (control model) were compared as a quantitative means of discerning if the anomaly was reliably detectable (i.e., outside the bounds of common dispersion data uncertainty). Those models categorized as containing a detectable anomaly, based on their experimental dispersion data, were further studied to determine if the dispersion data could be inverted to accurately resolve the anomaly's size, stiffness, and depth. To rigorously perform the inversions, the procedures recommended by the surface wave inversion

workflow SWinvert were adopted. These inversion procedures involve using multiple large-scale global-search inversions to address the problem's non-linearity and multiple layering parameterizations to address the problem's non-uniqueness. Following the inversion process, the shear wave velocity (Vs) profiles from the single "best" trial model associated with each layering parameterization were compared to the 1D Vs profiles from the centerline of the true/control model using an error function to quantitatively assess the ability of the MASW method to accurately resolve subsurface anomalies. In this study, anomalies with lateral extents less than approximately ½ the MASW array length located at depths greater than 5 m could not be resolved accurately by using MASW, even when the anomalies were relatively thick (> 2 m) and the impedance contrasts were notably high (> 2). The ability of MASW to detect an anomaly of a given size, stiffness, and depth is summarized in normalized figures, which are intended as a feasibility tool for those seeking to use MASW for anomaly detection.

Table of Contents

List of Tables

List of Figures

Chapter 1: Introduction

1.1. Overview

In-situ soil characterization with non-invasive surface wave methods has been widely used in past decades because they are relatively inexpensive and, perhaps erroneously presumed, easy to perform. Of these methods, the multichannel analysis of surface waves (MASW) method (Park et al., 1999; Foti, 2000) is one of the most common. Although this method is typically used to develop one-dimensional (1D) subsurface shear wave velocity (Vs) profiles, an area of particular interest is the application of MASW for anomaly detection.

MASW, as with other surface wave methods, involves three general steps: data acquisition, data processing, and inversion. Regarding data acquisition; MASW involves recording actively generated surface waves as they travel down a linear array of receivers. The array of receivers can vary in number (generally between 12 and 96) and spacing (generally between 0.5 and 5 m). Because it is believed the length of the receiver array governs the data's horizontal resolution, care should be taken when determining appropriate parameters to use while testing (Park 2005). Furthermore, the length of the array should also be chosen based on the desired depth of investigation. It is typical to choose an array length that is at least twice the investigation depth, or equal to the maximum desired wavelength (Foti et al. 2018). Additionally, a seismic source with appropriate frequency bandwidth should be chosen based on desired testing depths due to the relationship between depth of penetration and the surface wave frequency. Multiple shot offsets (i.e., the distance from the source to the nearest receiver in the array) may be used to improve gathered data (Foti et al. 2018). It is also important to choose proper shot offsets for the mitigation of near-field effects.

Regarding data processing; the recorded time histories gathered by the MASW array can then be analyzed to obtain measurements of the site's dispersion characteristics. This is completed by using any number of various two-dimension wavefield transformations, with the simplest being a two-dimensional Fourier transform to the frequency-wavenumber (i.e., f-k) domain (Nolet and Panza 1976). The points of maximum power of this two-dimensional transformation represent a measurement of the surface waves' dispersion characteristics, and these measurements are typically represented by plotting phase velocity as a function of frequency. The variation of surface wave phase velocity as a function of frequency or wavelength is typically referred to as a dispersion curve. However, it is probably more appropriate to refer to it as experimental dispersion data.

Regarding inversion; the purpose of surface wave inversion is to find the 1D subsurface model(s) with layer thicknesses (H), shear wave velocity (Vs), compression wave velocity (Vp), and mass density (ρ) whose solution to the analytical forward problem (i.e., theoretical dispersion curve) best matches the experimental dispersion data. Of particular importance is the determination of the subsurface Vs profile, as it has the greatest sensitivity in the forward problem and importance in engineering practice. To assess the goodness-of-fit between a potential model's theoretical dispersion curve, as calculated through the forward problem (Thomson, 1950; Haskell, 1953), and the experimental dispersion data, inversion requires the definition of a dispersion misfit value. The dispersion misfit value is most typically a L2 norm of error, or some normalized version thereof. In order to find the best match between a candidate model's theoretical dispersion curve and the experimental dispersion data, various inversion algorithms have been proposed to alter the model properties. Once a model has been found whose theoretical dispersion curve closely matches the experimental dispersion data, it can be inferred that

the model, and most importantly its Vs profile, is an acceptable representation of the subsurface. However, this process is not unique and care must be exercised to obtain realistic representations of the subsurface (Cox and Teague, 2016; DiGiulio et al., 2012, Vantassel and Cox, 2020).

Although the MASW method is typically used to develop 1D Vs profiles, an area of particular interest is the application of MASW for anomaly detection, wherein a number of 1D Vs profiles are interpolated to obtain a pseudo-2D representation of the subsurface. Such applications include investigation of weak zones in levee systems (Rahimi et al. 2018), detection of karst conduits (Debeglia et al. 2006), detection of voids near the surface (i.e., < 3 m) (Nolan et al. 2011), shallow man-made tunnel detection (i.e., < 3 m) (Sloan et al. 2013), delineation of sink-holes, voids, and mines (Sloan* et al. 2015; Ivanov et al. 2016) identification of the location of a dam's compacted core (Hock et al. 2007), and evaluation of unknown subsurface bridge foundations (Mahvelati and Coe 2017). The successful application of surface wave methods for anomaly detection relies on the anomaly being within the vertical and horizontal detection limits, which depend on a number of factors, including: (a) the receiver spacing and length of the MASW array, (b) the minimum and maximum frequencies/wavelengths resolved during testing, (c) the size of the anomaly, and (d) the stiffness contrast of the anomaly relative to the surrounding materials (Xia et al. 1999; Park 2005; Ivanov et al. 2008). However, successful detection of an anomaly at the dispersion processing stage does not necessarily equal successful resolution of the anomaly during the inversion stage. Accurately resolving subsurface anomalies can be challenging for surface wave methods due to: (1) the 1D nature of the forward problem used to calculate theoretical dispersion curves from a trial subsurface model, whereas anomalies inherently induce 2D/3D variability in the subsurface, and (2)

the non-uniqueness of surface wave inversion, which results in a number of candidate models that can fit the experimental data equally well.

This paper presents the results of attempts to detect and resolve subsurface anomalies using the MASW method. The ability of the MASW method to detect and resolve subsurface anomalies will be discussed using quantitative and qualitative approaches. The detailed analysis and workflow regarding the ability of MASW method to detect and resolve subsurface anomalies will be discussed in the corresponding chapters.

1.2. ORGANIZATION OF THESIS

This thesis contains 4 chapters. A brief description of each chapter is below.

- Introduction (Chapter 1)
- Chapter 2 is a manuscript of a conference paper titled "Limitations of the multichannel analysis of surface waves (MASW) method for subsurface anomaly detection" that has been accepted to the 6th International Conference on Geotechnical and Geophysical Site Characterization that was going to be held in Budapest, Hungary in September 2020 (postponed to 2021 due to Covid-19).
- Chapter 3 is a manuscript of a conference paper titled "Ability of the multichannel analysis of surface waves method to resolve subsurface anomalies" that has been accepted to the International Foundations Conference and Equipment Expo that will be held in Dallas, TX in May 2021.
- Conclusions and Recommendations (Chapter 4)
- Appendix A: Additional Summary Plots of Relative Misfit and Inversion Results

1.3. RESEARCH OBJECTIVES

The detailed objectives of this study are:

- To assess the ability of the MASW method to detect anomalies of varying size, stiffness, and depth.
- To evaluate the ability of the MASW method to resolve anomalies of varying size, stiffness, and depth.
- To understand the importance of layering parameterization and its effects on the surface wave inversion results.

Chapter 2: Limitations of the MASW Method for Subsurface Anomaly Detection

This chapter contains a conference paper manuscript that has been accepted for presentation at the 6th International Conference on Geotechnical and Geophysical Site Characterization in September 2020 (postponed to 2021 due to COVID-19). The full citation is listed below:

Crocker, A. J., Ugur, A., Vantassel, J., & Cox, B. (2020). Limitations of the multichannel analysis of surface waves (MASW) method for subsurface anomaly detection. Accepted to the 6th International Conference on Geotechnical and Geophysical Site Characterization in Budapest, Hungary. 7-11 September 2020 (postponed to 2021 due to COVID-19)

As second author, I was responsible for approximately 10% of the project planning, 50% of the data acquisition, 50% of the data processing, and 30% of the results interpretation.

ABSTRACT

This study assesses the practical limitations of using the multichannel analysis of surface waves (MASW) method for detecting subsurface anomalies. The sensitivity of MASW dispersion data to the presence of subsurface anomalies is examined through various two-dimensional (plane-strain) finite-difference elastic wave-propagation simulations. These simulations were performed on models with anomalies of varying size, stiffness, and depth. The misfit between the dispersion data from a model with an anomaly (treatment model) and the same model without an anomaly (control model) were compared as a quantitative means of discerning if the anomaly was reliably detectable (i.e., outside the bounds of common dispersion data uncertainty). The ability of MASW to detect an anomaly of a given size, stiffness, and depth is summarized in normalized figures, which are intended as a feasibility tool for those seeking to use MASW for anomaly detection.

Keywords: surface waves; site characterization; multichannel analysis of surface waves; anomaly detection

2.1 INTRODUCTION

In order to perform geotechnical design, it is necessary to obtain accurate information regarding the characteristics of the subsurface, which include the subsurface material's physical properties and spatial variability. Unfortunately, obtaining extensive information with the current state-of-practice remains highly impractical. This is especially true when using invasive methods, such as drilling boreholes, due to the time and cost involved. As a result of the need for more complete in-formation in recent years, non-invasive methods, especially those capable of producing two- and three-dimensional subsurface images, have seen a marked increase in their popularity. These methods include re-fraction tomography, reflection tomography, electrical resistivity imaging (ERI), full-waveform inversion (FWI), and the multichannel analysis of surface waves (MASW) method (J. Xia et al. 2004; Hirsch et al. 2008; Rahimi et al. 2018; Mirzanejad and Tran 2019). This study will focus on the MASW method due to its wide-spread use.

The MASW method (Park et al. 1999) was developed as a relatively inexpensive and efficient non-invasive test which us-es the propagation of surface waves to evaluate subsurface stiffness. MASW involves recording actively generated surface waves as they travel down a linear array of receivers. These recordings are then processed to obtain surface wave dispersion data using one of several two-dimensional (i.e., time and space) transformations (Nolet and Panza 1976; Zywicki 1999). This estimate of the site's surface wave dispersion characteristics (i.e., the variation of surface wave velocity as a function of frequency or wavelength) is often referred to as the experimental dispersion curve. This measurement of the site's dispersion is generally not the end goal, but rather is inverted to produce an estimate of the site's one-dimensional shear-wave velocity (Vs) profile. This profile is generally believed to be representative of the soil beneath the center of the array

(Jianghai Xia et al. 2000). Multiple 1D Vs profiles may then be combined and interpolated to form a pseudo-2D image of the subsurface.

This process for using MASW to develop a pseudo-2D subsurface image has shown varying degrees of success in literature, particularly regarding the detection of subsurface irregularities. For example, when comparing the MASW method to seismic refraction and ERI, Groves et al. (2011) found that MASW testing was the most successful at detecting three distinct soil layers at the near-surface (i.e., the top 4 m) and that it was able to detect an increase in stiffness due to a large till layer located approximately 4.6 to 10.7 m deep across the site, but provided an inaccurate estimate of the depth to that layer. In contrast, ERI was shown to provide the most accurate estimate to the soil-till interface. Alternatively, Ismail et al. (2014) found that the MASW method was not able to provide high vertical or lateral resolution of soil layers compared to the shear-wave reflection method but provided relatively better Vs measurements at a lower time and cost. Mahvelati and Coe (2017) found that using MASW testing to detect the geometry of un-known bridge foundations could produce mixed results. Specifically, the lateral extent of the bridge's foundation was relatively accurate while the depth and thick-ness were smaller than expected based on prior knowledge regarding the foundation's design. Nolan et al. (2011) used a shallow, man-made void to illustrate the accuracy of MASW testing. They found that it was possible to detect a subsurface anomaly using MASW, although there was limited resolution in both the vertical and lateral geometry of the void. Pan et al. (2019) analyzed the ability of MASW testing to detect lateral heterogeneity by creating a synthetic model containing a checkerboard pattern of stiff and soft soil. They dis-covered that MASW had poor resolution and the checkerboard model could not be recovered, whereas using the same model analyzed with FWI allowed for much higher resolution.

Given the mixed conclusions regarding the MASW method's ability to detect and accurately resolve underground irregularities, this paper seeks to evaluate the possibility of detecting subsurface anomalies by using a variety of synthetic models and the MASW method. In this study, MASW-style testing is performed numerically on a control model without an anomaly and a number of treatment models containing anomalies of varying size, location, and stiffness. Each model contains a simulated array of receivers and multiple source locations based on testing parameters commonly found in literature. As a simplification each anomaly was rectangular in shape, homogenous, and centered underneath the array. The 2D finite-difference code DENISE was used to simulate the MASW wavefield (Köhn et al. 2012). The experimental waveforms were then processed using standard MASW techniques to estimate an experimental dispersion curve. The misfit between the experimental dispersion curves from each treatment and control model pair was then calculated. The misfit values were then summarized in figures for use as a guide to quantify the feasibility of detecting a subsurface anomaly.

2.2 METHODOLOGY

2.2.1 MASW Methodology

The MASW method relies upon the propagation of surface waves (Rayleigh or Love) to evaluate subsurface soil stiffness. The velocity (v) of the waves as they travel through the subsurface is dependent not only on the properties of the material through which they propagate, but also on their frequency (f). This dependence of the waves' phase velocities on frequency is called dispersion. The dispersive nature of surface waves is useful for site characterization because the depth of penetration into the ground may be thought of as a function of a wave's measured wavelength ($\lambda = v/f$). A rough estimate of the depth to which the wave can "see" (i.e., dmax) is generally approximated to be about

half its wavelength ($\lambda/2$). Therefore, given that frequency and wavelength have an inverse relationship, it follows that a low f corresponds to a longer λ and vice versa. Consequently, higher frequencies will propagate at velocities corresponding to shallower layers, while lower frequencies will propagate at velocities that are influenced by both the shallow and deeper layers, as illustrated schematically in Fig. 2.1.

To perform MASW testing, a seismic source is operated in-line with the axis of the array of receivers to generate surface waves, which are then recorded by the array of receivers. The array of receivers can vary in number (generally between 12 and 96) and spacing (generally between 0.5 and 5 m). Because it is believed the length of the receiver array governs the data's horizontal resolution, care should be taken when determining appropriate parameters to use while testing (Park 2005). Furthermore, the length of the array should also be chosen based on the desired depth of investigation. It is typical to choose an array length that is at least twice the investigation depth, or equal to the maximum desired wavelength (Foti et al. 2018). Additionally, a seismic source with appropriate frequency bandwidth should be chosen based on desired testing depths due to the relationship between depth of penetration and the surface wave frequency. Multiple shot offsets (i.e., the distance from the source to the nearest receiver in the array) may be used to improve gathered data (Foti et al. 2018). It is also important to choose proper shot offsets for the mitigation of near-field effects.

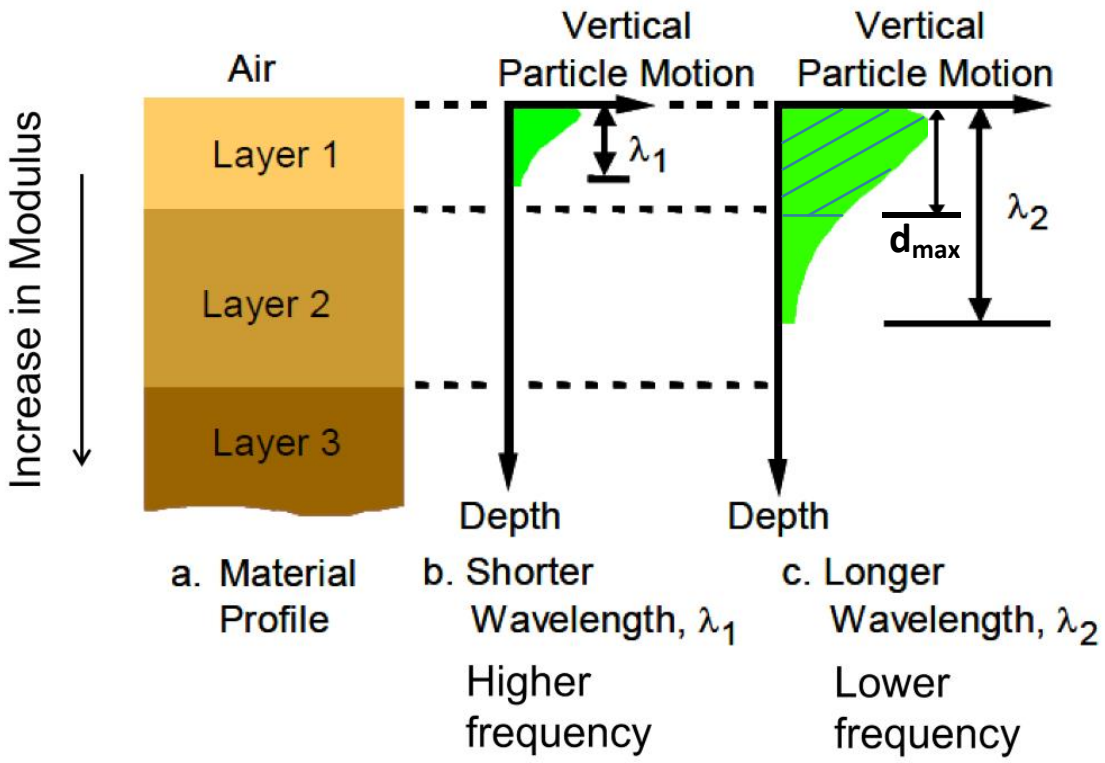

Figure 2.1: The relationship between surface wave vertical particle motion, wavelength, and frequency are shown. Note that shorter wavelengths correspond to higher frequencies, whereas longer wavelengths correspond to lower frequencies. Fig. 2.1b shows one wavelength, while Fig. 1c shows dmax, or λ/2, which is the "visible" depth [modified from (Stokoe et al. 2006)].

The recorded time histories gathered by the array can then be analyzed to obtain measurements of the site's dispersion characteristics. This is completed by using any number of various two-dimension wavefield transformations, with the simplest being a two-dimensional Fourier transform to the frequency-wavenumber (i.e., f-k) domain (Nolet and Panza 1976). The points of maximum power of this two-dimensional transformation represent a measurement of the surface waves' dispersion, and these measurements are typically represented by plotting phase velocity as a function of frequency. Ultimately, these measurements of phase velocity are inverted to obtain a 1D Vs profile. If multiple

MASW arrays were set up in close proximity to one another, their resulting 1D Vs profiles can be contoured to produce a pseudo-2D and, in certain cases, a pseudo-3D image. The purpose of this work is to primarily assess the first stage of this process (i.e., the ability to detect an anomaly at the dispersion stage). However, it should be noted that detecting an anomaly at the dispersion stage does not imply that it can be accurately resolved during the inversion phase. Accurately resolving the depth, size, and stiffness of an anomaly via inversion is a much more complicated problem due to the non-unique nature of inverse problems.

2.2.2 Model Development

To simulate MASW testing, DENISE, a 2D plane-strain finite-difference program, was used (Köhn et al. 2012). This program simulates wave propagation by solving the 2D wave equation for an elastic medium. Each model was 256 m in length and 64 m in depth and discretized into square 0.25 m elements. The order of the finite-difference operator was eight, and PML boundary conditions were applied to the bottom and side faces of each model. In particular, the width of the absorbing frame was 25 gridpoints, and the frequency within the PML was 10 Hz. The damping velocity was set to 1,500 m/s, and the degree of the damping function was 2. The remaining inputs for each model included user-defined receiver spacing, array length, source type, and sampling parameters, which are detailed in Section 2.2.3.

Each control model (i.e., with no anomaly present) was generated to contain a uniform body of soil (i.e., a half-space) with a constant density (ρ), Poisson's ratio (ν), and Vs. Two control models were considered, where one had Vs equal to 150 m/s and the other 300 m/s, while ρ and ν were held constant at 2,000 kg/m3 and 0.33, respectively.

Various anomalies were then placed into each half-space to create the treatment models. These anomalies were selected to be noticeably softer/stiffer than the surrounding material. Specifically, impedance contrasts, defined as the ratio of the anomaly Vs to the half-space Vs, of 1.5, 2.0, and 5.0 were used for models containing a stiff anomaly, whereas values of 0.20, 0.50, and 0.67 were used for soft anomalies. This means for a half-space Vs of 150 m/s, stiff anomalies had Vs equal to 225, 300, and 750 m/s, while soft anomalies were created with Vs equal to 30, 75, and 100 m/s. Similarly, for a half-space Vs of 300 m/s, stiff anomalies had Vs equal to 450, 600, and 1,500 m/s, while soft anomalies were created to have values of Vs equal to 60, 150, and 200 m/s.

Each anomaly was centered under the array to represent a single snapshot in space representative of a traditional 2D MASW survey. An anomaly directly under the center of the array should yield the best opportunity to accurately detect and resolve it. To examine the sensitivity of MASW to the width of an anomaly, various lateral extents between 1 and 36 m were used. To test the vertical resolution of MASW, anomalies were placed at top depths increasing from 2 to 20 m. Anomaly thicknesses of 1, 2, and 4 m were also considered to assess the detectability of various irregularities that may be present in soil. Fig. 2.2 is a schematic of a typical treatment model with the previously mentioned variables listed for ease of understanding.

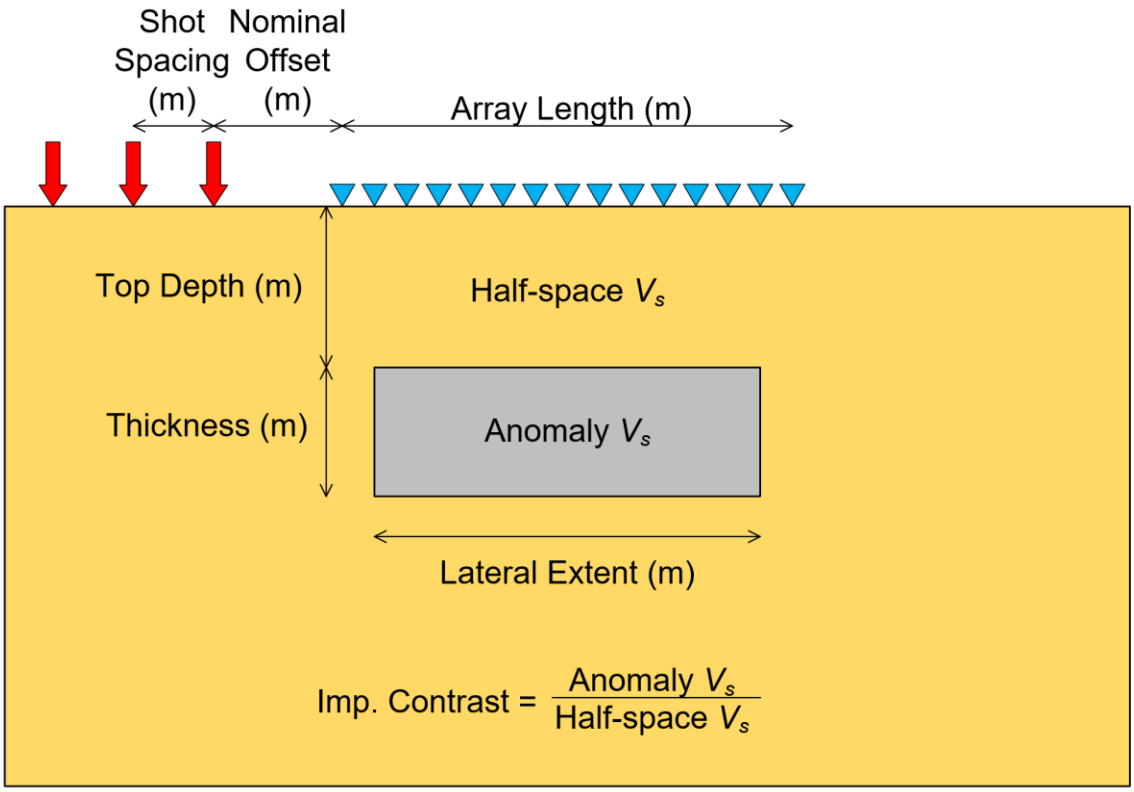

Figure 2.2: A general schematic for each treatment model is shown. The half-space and anomaly shear-wave velocities were varied to create a range of impedance contrasts, while the top depth, thickness, and lateral extent of each anomaly were varied to represent a set of possibilities that may be encountered during field testing. Roughly 300 models were created for each unique impedance contrast and half-space Vs pairing, such that over 3,000 models in total were created for all impedance contrasts.

Additionally, to more easily reference models, each model was assigned a unique identification code. Each code consists of a string of letters and numbers, which are representative of each variable and its value, as shown in Table 2.1. For example, given an anomaly that is 36 m wide, 4 m thick, at a depth of 20 m, and with an impedance contrast of 0.67 placed in a half-space with Vs equal to 150 m/s, the model may be identified as I0.67 H150-T4-D20-L36. Because over 3,000 unique models were generated for this study,

Table 2.1: Summary of model variables with associated values

Variable	Acronym	Values
Impedance Contrast	I	0.67, 0.2, 0.5; 1.5, 2.0, 5.0
Half-space Vs (m/s)	H	150, 300
Anomaly Thickness (m)	T	1, 2, 4
Top Depth (m)	D	2 – 20
Lateral Extent (m)	L	1, 4, 6, 10, 14, 19, 25, 30, 36

this naming convention was adopted so that each model has a descriptive identifier that may be quickly referenced.

2.2.3 Model Testing Parameters

To ensure the 2D MASW testing was being per-formed in conformance with the standard of practice, a literature review was performed to summarize a "typical" test configuration. The literature review examined parameters such as array lengths, receiver spacings, and source frequency content. When analyzing various case studies, it was determined that 24 receivers spaced at approximately 1 m (J. Xia et al. 2004; Ivanov et al. 2009; Mohamed et al. 2013; Suto et al. 2014; Mahvelati and Coe 2017) were used to form an array. A minority of studies used 24 receivers with a receiver spacing greater than 1 m, though this was done explicitly in the hope of obtaining longer wavelengths and therefore deeper testing depths (Debeglia et al. 2006; Shakir et al. 2013; Rahimi et al. 2018). Others chose to use a constant 1 m receiver spacing but utilized more than 24 receivers to similarly create longer array lengths (Ivanov et al. 2006; Groves et al. 2011; Nolan et al. 2011). Therefore, to be consistent with the majority of case histories, each simulation used 24 receivers spaced at 1 m for a total array length of 23 m.

In field tests, the cheapest and most commonly used seismic source is the sledgehammer. Sledgehammers weighing at least 5 kg can be used to obtain data across a relatively large frequency band, and many case studies have utilized sledgehammers with varying degrees of success (J. Xia et al. 2004; Debeglia et al. 2006; Mohamed et al. 2013; Suto et al. 2014; Mahvelati and Coe 2017; Rahimi et al. 2018). However, this source typically does not provide much energy at lower frequencies (less than 8 Hz), which means more powerful sources, such as an accelerated weight drop or vertically operated shaker, should be used if lower frequencies are desired (Foti et al. 2018). Ultimately, it was decided that the simulations should be conducted under very favorable source conditions in order to provide the best chance at detecting anomalies, such that frequencies from 5 Hz – 100 Hz were considered for all models. Multiple sources were tested until data were obtained within this bandwidth, and it was determined that the desired source bandwidth was acquired using a fifth-order Butterworth filtered spike wavelet. A timestep of 0.02 ms was used for a total record time of 3 s, and the output waveforms were then downsampled to 400 Hz.

After determining the array length and bandwidth of the seismic source, various shot locations were analyzed to determine which location(s) would provide the highest quality dispersion data. Near-field effects, which occur when surface waves have not yet fully developed before being recorded by a receiver, are caused by having a small offset between the array and the source. To avoid near-field effects, it is recommended that a source offset of at least three to five times the receiver spacing should be used (Foti et al. 2018). In this study, an offset of ten times the receiver spacing, or -10 m, was used for the closest shot location. This was due to a shot location of -5 m yielding clear near-field data when compared to further offsets. It was determined that shot offsets of -10, -15, -20, and 25 m provided acceptable data with-out obvious near- or far-field effects for the majority

of the models. Given that the models were known to be symmetric, shots were only required off one side of the array. A summary of testing parameters used in this study are included in Table 2.2.

Table 2.2: Summary of model testing parameters

No. of receivers	24
Receiver spacing	1 m
Array length	23 m
Type of source	Spike wavelet, 0-15 Hz
Sampling frequency	400 Hz
Record length	3 s
Nominal offset	-10 m
Source spacing	5 m

2.3 DATA ANALYSIS

2.3.1 Processing Dispersion Data

After running the control and treatment models, the simulated waveforms were transformed in the frequency domain using the frequency domain beam former (FDBF) method (Zywicki 1999). The FDBF used an inverse-amplitude weighting scheme with a cylindrical steering vector. All calculations were performed over a frequency bandwidth of 1 – 200 Hz. After the transformation, the maximum spectral peak for each frequency was automatically chosen and plotted to form dispersion curves. The dispersion curves for multiple offsets were then plotted together and statistically combined to form a mean dispersion curve with uncertainty following the recommendations of (B. R. Cox and Wood 2011). Fig. 2.3a-b show examples of a dispersion image for a -10 m offset for models com-

posed of a half-space with Vs equal to 300 m/s and an anomaly that is 2 m thick, 36 m wide, at a top depth of 5 m, and with a Vs of 60 m/s and 1,500 m/s (models I0.20-H300-T2-D5-L36 and I5.00-H300-T2-D5-L36), respectively. The hollow white circles identify the peak energy at each frequency. Fig. 2.3c-d show the combined dispersion data for all shot offsets for each model. It should be noted that the dispersion curves in Fig. 2.3c-d have not yet been processed to remove data points from higher modes, outliers, and data beyond the 5 Hz – 100 Hz frequency bandwidth.

Prior to binning dispersion data and calculating phase velocity statistics (mean and standard deviation), clear outliers were removed from each data set, as is standard for MASW. This was completed by visually determining which data significantly deviated from the mean of the dispersion data for a given frequency. Da-ta below 5 Hz and above 100 Hz were omitted to pro-vide a consistent, but optimistic, frequency bandwidth for all models. To ensure the dispersion data from all models were provided at the same frequencies, each set of dispersion data was logarithmically resampled be-tween 5 and 100 Hz with 100 points.

When viewing the dispersion curves, higher mode trends were sometimes visible in addition to the fundamental mode. Although the fundamental mode alone is typically identified for use in inversions during 2D MASW processing, higher mode data can also provide useful information regarding the soil stratigraphy. In this study, not all models exhibited the presence of higher mode data. Therefore, an effort was made to consistently process the dispersion data in an attempt to recover a dispersive trend as close to the fundamental mode as possible. Although, in some cases, this required including dispersion data points along a trend of super-posed higher modes. To illustrate this, Fig. 2.3e-f show the dispersion data from Fig. 2.3c-d after trimming and calculating statistics. Fig. 2.3e-f

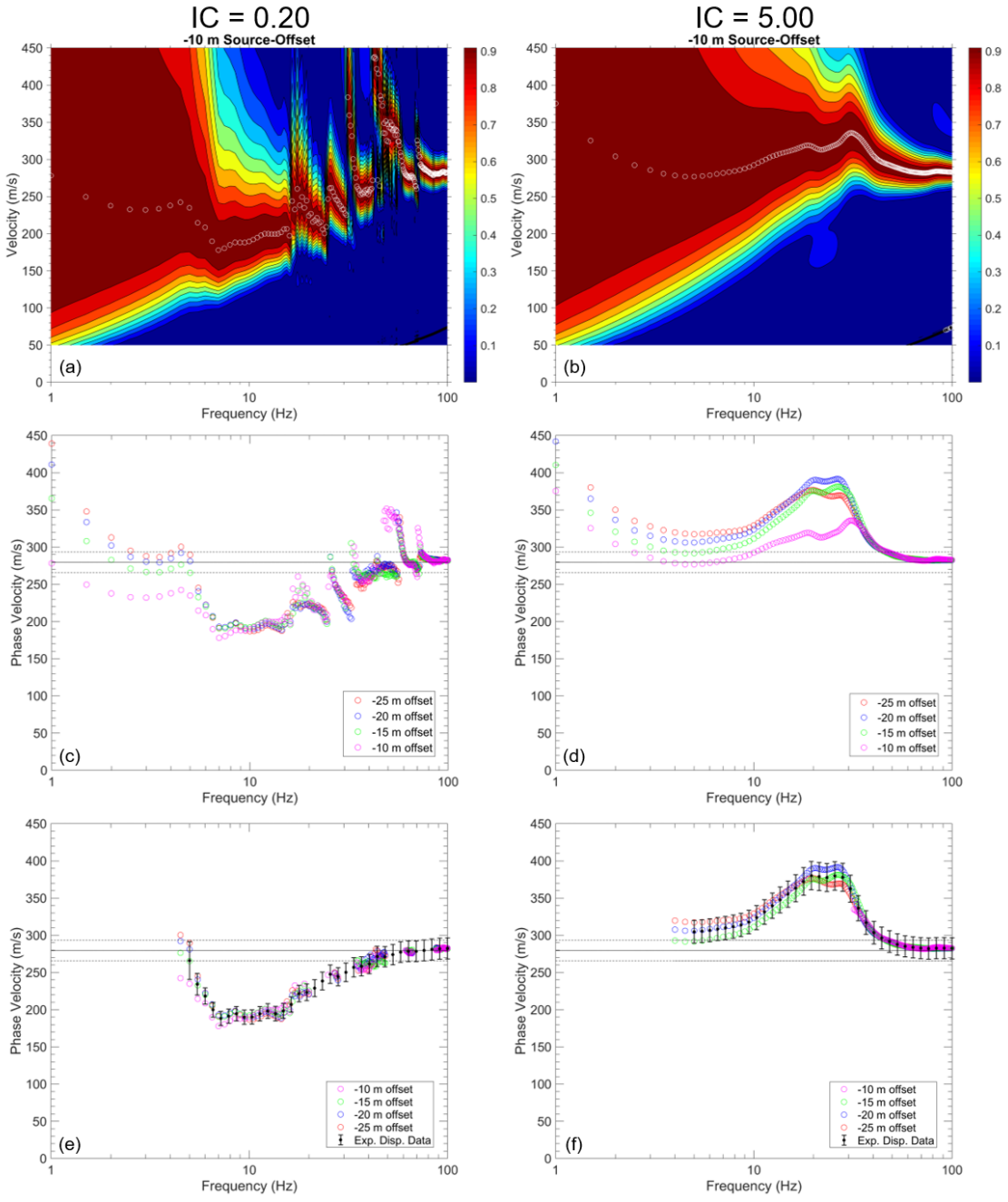
IC = 0.20
-10 m Source-Offset
IC = 5.00
-10 m Source-Offset
Velocity (m/s)
Frequency (Hz)
(a)
(b)
Phase Velocity (m/s)
(c)
(d)
-25 m offset
-20 m offset
-15 m offset
-10 m offset
(e)
(f)
-10 m offset
-15 m offset
-20 m offset
-25 m offset
Exp. Disp. Data

Figure 2.3: Dispersion data for two models containing an anomaly that is 2 m thick, 36 m wide, and at a top depth of 5 m. The shear-wave velocity of the surrounding soil is 300 m/s while the anomaly's shear-wave velocity is 60 m/s (left column) or 1,500 m/s (right column). Specifically, the model shown in the left column is model I0.20 H300-T2-D5-L36, while the right column is model I5.00 H300-T2-D5-L36. (a-b) show the corresponding dispersion images for the closest shot offset with peak energies identified as white hollow circles at each frequency. (c-d) show the raw dispersion data before trimming and calculating statistics. In both (c) and (d), the presence of higher modes is clearly visible. (e-f) show the same dispersion data from (c-d) after trimming and calculating statistics to obtain a lower-bound "fundamental mode" from the superposed higher modes. The solid black line in (c-f) represents the theoretical phase velocity of the half-space, while the dashed lines represent an assumed 5% coefficient of variation on phase velocity.

show the trimmed dispersion curve with the lower-bound trend that is presumably close to the fundamental mode, but should more accurately be termed a superposition of modes.

2.3.2 Calculating Relative Misfit

Once the dispersion curves were processed for all models, relative misfits between the control models (i.e., the half-space models) and their associated treatment models were calculated using the L1 norm of dispersion residuals. Although the L2 norm is more commonly used, various studies have found that using the L1 norm is equally applicable. Specifically, Brossier et al. (2010) found that using an L1 norm with FWI provides more accurate 2D Vs maps relative to the L2 norm, while Chambers et al. (2006) found that inverting electrical resistivity tomography data with L1 norm implementations allowed for better resolution when analyzing sharp boundaries between materials with high resistivity contrasts. Additionally, the L1 norm has an established low sensitivity to outliers when compared to the L2 norm. Therefore, the L1 norm misfit was deemed to be more suitable for this study. The equation is as follows:

$$M_{dc,rel} = \sum_{i=1}^{n_f} \frac{|x_{ci} - x_{ti}|}{\sigma_{ci} n_f} \quad (2.1)$$

where xci is the Rayleigh wave phase velocity of the control model at frequency fi, xti is the Rayleigh wave phase velocity of a treatment model at fi, σci is the standard deviation of the control model's dispersion data at fi, and nf is the number of frequency samples being considered. From Eq. (2.1), it can be deduced that a misfit of one would correspond to a treatment dispersion curve that is on average one standard deviation away from the mean of a control dispersion curve. Therefore, a misfit less than one indicates a treatment model's dispersion curve is on average within the bounds of uncertainty of the control model's dispersion curve and not easily distinguishable from the control model. Note that a constant 5% COV was used to estimate the control models' dispersion uncertainty. Several blind studies have shown that experimental dispersion data can typically be re-solved within 5% - 10% COV (B. R. Cox et al. 2014; Garofalo et al. 2016). The lower COV value was chosen to again provide more favorable circumstances for detecting the anomalies in the models.

2.4 Results and Discussions

Using Eq. (2.1), relative misfits were calculated be-tween each treatment model and its corresponding control model. An example of a set of three treatment models compared to a control model is shown in Fig. 2.4. In this case, the control model consists of a half-space with Vs equal to 150 m/s. Three different treatment models containing anomalies that are 1 m thick, 36 m wide, and with a Vs of 30 m/s were chosen. These models were selected so that a comparison between three different top depths could be made (specifically, models I0.20-H150-T1-D2-L36, I0.20-H150-T1-D6-L36, and I0.20-H150-T1-D14-L36 were chosen). For an anomaly placed at a depth of 2 m, 6 m, and 14 m, mis-

fit values were measured as 4.4, 1.4, and 0.5, respectively. Fig. 2.4 visually demonstrates that increasing misfit values correspond directly to larger deviations between the control model and treatment models. A treatment model with a shallow anomaly and a misfit value of 4.4 is easily detectable; however, a treatment model with a deeper anomaly and a misfit of 0.5 is not easily detect-able outside the bounds of typical dispersion data un-certainty. Additionally, these dispersion curves were plotted with respect to wavelength rather than frequency to better illustrate the effects the depth of the anomaly has on misfit values. The correspondence between wavelength and depth is apparent in Fig. 2.4 as the presence of a shallow anomaly (i.e., 2 m) causes the treatment model's dispersion curve to deviate from that of the control model at smaller wavelengths. However, for this same shallow anomaly the dispersion data begins to return to the half-space velocity at long wavelengths as they "see" through the anomaly and into the half-space beneath. Note that the misfit of each model is highly non-linear with depth. In particular, the difference in the misfit when the anomaly is at 2 m is significantly (by almost a factor of 3 times) larger than when it is at 6 m with the same being true for the 6 and 14 m depths. This non-linear relationship between depth and misfit (i.e., whether or not the anomaly is detectable) is discussed further when analyzing the trends in misfit values for all models.

After processing over 3,000 unique models, figures were created to summarize the trends observed in the misfit values (refer to Fig. 2.5-10). In these figures, the lateral dimension of each anomaly was normalized with respect to the length of the array used in the simulated tests. To summarize the results succinctly, plots were created for each unique combination of impedance contrast and half-space Vs as no acceptable form of velocity normalization could be found to combine all results. This was due in part to the observation that with all other parameters held constant (i.e., depth, thickness, and impedance contrast), absolute Vs of the half-space and anomaly are important and result in vastly different misfit

values. These differences in misfit are believed to stem from non-equal wavelengths across models. Since wavelength is a function of velocity and frequency, it follows that higher velocities will result in larger wavelengths for similar frequencies and thus the potential to detect an anomaly with depth will vary de-pending on the velocities present at a site. To illustrate these differences, the overall maximum and minimum wavelengths (λ_{max} and λ_{min}, respectively) have been shown for each figure. Each figure was further separated by anomaly thickness and half-space (HS) velocity for ease of viewing. For plotting purposes, misfit values over 3.0 were all assigned the same color scale, as values of 3.0 and higher represent clearly detectable anomalies. Additionally, Table 2.3 has been provided, which summarizes the key findings of each set of figures.

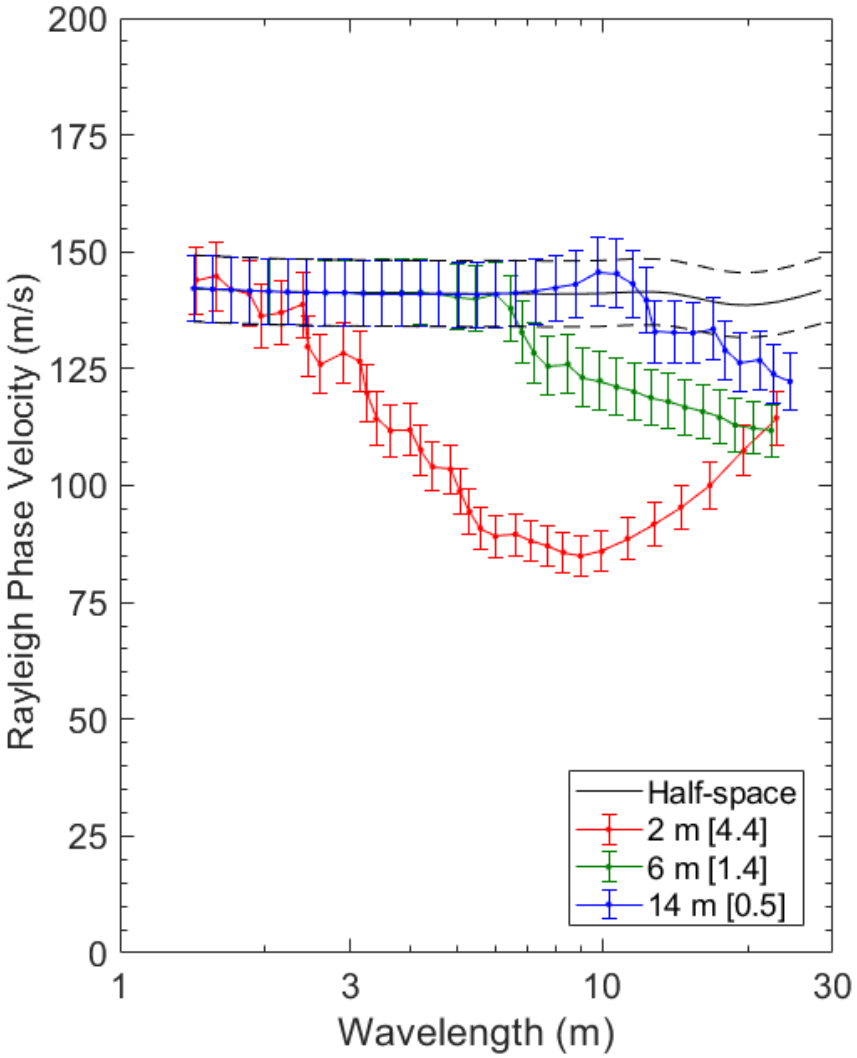

Figure 2.4: Comparison of dispersion data for models containing an anomaly that is 1 m thick and 36 m wide at varying top depths (2 m, 6 m, and 14 m). The shear wave velocity of the anomalies is 30 m/s while the surrounding soil has a shear wave velocity of 150 m/s. Note that as the top depth of the anomaly increases, the relative misfit values (indicated inside the legend in brackets []) for the respective dispersion curves decrease. The phase velocities are presented as a function of wavelength such that the trend regarding depth is more easily seen.

Each figure presents misfit values for a fixed impedance contrast as a function of the anomaly's top depth (vertical axis), normalized lateral extent (horizontal ax-is), HS

velocity, and anomaly thickness. A clear boundary at a misfit value of 1.0 was included in order to indicate the zone above which an anomaly will most confidently be detected. Specifically, the colors above the boundary line (the gradient from green to red) indicate that an anomaly within this zone is likely to be detectable, while the colors below the boundary line (the gradient of blue colors) indicate anomalies within this zone will be more difficult to detect. This is not to say that the blue zone represents that an anomaly is impossible to detect; rather, the blue zone represents that an anomaly cannot be detected with a high degree of confidence.

Fig. 2.5 shows the results for an impedance contrast of 0.67. Fig. 2.5a-c are for models generated with a half-space Vs of 150 m/s while Fig. 2.5d-f are for a half-space Vs of 300 m/s. Both rows are listed in order of increasing anomaly thickness, such that Fig. 2.5a-c and Fig. 2.5d-f are for anomalies that are 1, 2, and 4 m thick, respectively. From these figures, as expected, it is clear that an in-crease in anomaly thickness directly corresponds to an increase in the chance to detect it. The same is true with increasing lateral extent of the anomaly relative to the length of the array. However, despite the expected trends showing an increase in detectability for larger anomalies, the results for this impedance contrast indicate it may be more difficult than anticipated to easily detect anomalies. For example, a 1 m-thick anomaly must be longer than at least three-quarters of the array length to have a high chance of being detected, while a 4 m-thick anomaly must be longer than at least a quarter of the array length. Further, 1 m-thick anomalies can only be confidently detected up to 3 m deep, while 4 m-thick anomalies can only be confidently detected up to about 6 m deep. When comparing the change in half-space Vs between respective sets of models, it is shown that an increase in half-space Vs also corresponds to an increase in general detectability. This is believed to be related to the in-crease in the overall maximum wavelength present for each set of models. As previously

mentioned, higher velocities will result in longer wavelengths for a given frequency, which is shown in Fig. 2.5d-f where the maxi-mum wavelength present for each set of models is nearly double the maximum wavelength for the corresponding sets in Fig. 2.5a-c. Due to this, it is understandable that an increase in overall velocity at a given impedance contrast results in an increase in the possibility of deeper anomaly detection. These results are further tabulated in Table 3, such that trends in the maximum likely detectable depth as well as the minimum likely detectable size of an anomaly may be more easily visualized. It should be noted that the results listed in Table 2.3 are ap-proximate values and represent the boundaries of likely detection.

Fig. 2.6 presents similar misfit summary plots for models with an impedance contrast of 0.50. These results show that for a larger impedance contrast, the ability to detect anomalies increases. In particular, the depth at which a 1 m-thick anomaly can be detected has nearly doubled, which can be seen when comparing Fig. 2.5a and Fig 2.5d with Fig. 2.6a and Fig. 2.6d, respectively. Additionally, the size of a detectable anomaly is smaller. Like Fig. 2.5, the maximum wavelengths present in the high velocity models (Fig. 2.6d-f) are more than double the wavelengths present in similar sets of models with lower velocities (Fig. 2.6a-c), and as such, the maximum depth at which anomalies can be confidently detected is greater when higher velocities are present. This trend further supports the assertion that the wavelengths pre-sent for each set of models are directly related to the chance of detecting anomalies at increasing depths.

Fig. 2.7 presents the misfit values for an impedance contrast of 0.20. These figures are notably distinct from those shown previously in that Fig. 2.7a c show almost no change in the maximum depth at which an anomaly can be reasonably detected despite increases in thick-ness. Likewise, Fig. 2.7d-f show that increases in anomaly thickness do not show visible effects on the maximum depth of detectability, although this is at least partially due

to the misfit boundary of 1.0 extending beyond the depths used in this study. Regarding Fig. 2.7d-f, the absence of a maximum depth of detection is likely due to the data provided by high impedance contrasts. Although the maximum wavelengths measured for each set of models reveal that it is possible to detect anomalies at relatively large depths, the dispersion data obtained for each of these models was quite complicated with significant higher modes. This meant that, despite using a lower-bound dispersion trend from superposed modes, the dispersion curves for various treatment models were still significantly distinguishable from that of the control model. Therefore, it was found that for models containing higher velocities and an impedance contrast as significant as 0.20, the chance of detecting anomalies in general is more probable than compared to models containing lower velocities. Based on Fig. 2.7d-f, it was assumed that Fig. 2.7a c would also show an in-crease in misfit as thickness increases. However, the maximum depth for the misfit boundary of 1.0 is shown to remain relatively constant for each thickness. This is likely due to the maximum wavelengths shown in Fig. 2.7b and Fig. 2.7c as they reveal that the depth of detection should be roughly 7 and 6 m, respectively, if using an estimate of $\lambda/2$. Therefore, for these two sets of models, it is reasonable that the maximum depth of detection does not significantly increase with changes to anomaly thickness as the anomaly, regardless of its thickness, is already nearly undetectable at this depth.

Fig. 2.8-10 present the misfit values for models containing an anomaly that is stiffer than the surrounding half-space. When comparing each set of models, it is clear that overall, it is more difficult to detect a stiff inclusion as opposed to a soft one. In particular, Fig. 2.8 shows that it is difficult to detect a 1 m-thick anomaly regardless of the half-space Vs. Both the 2 m- and 4 m-thick anomalies are shown to be detectable, but when compared to Fig. 2.5b-c, the boundary at which a misfit of 1.0 is pre-sent is shallower for models containing a stiff anomaly. In terms of an anomaly's lateral extent, the minimum size

required for an anomaly to be detectable does not significantly change depending on whether the anomaly is soft or stiff relative to the surrounding soil (compare for example Fig. 2.5 and Fig. 2.8). Fig. 2.9 presents misfit values for models with an impedance contrast of 2.0, again illustrating that stiff anomalies are overall more difficult to detect than soft anomalies when compared with Fig. 2.6.

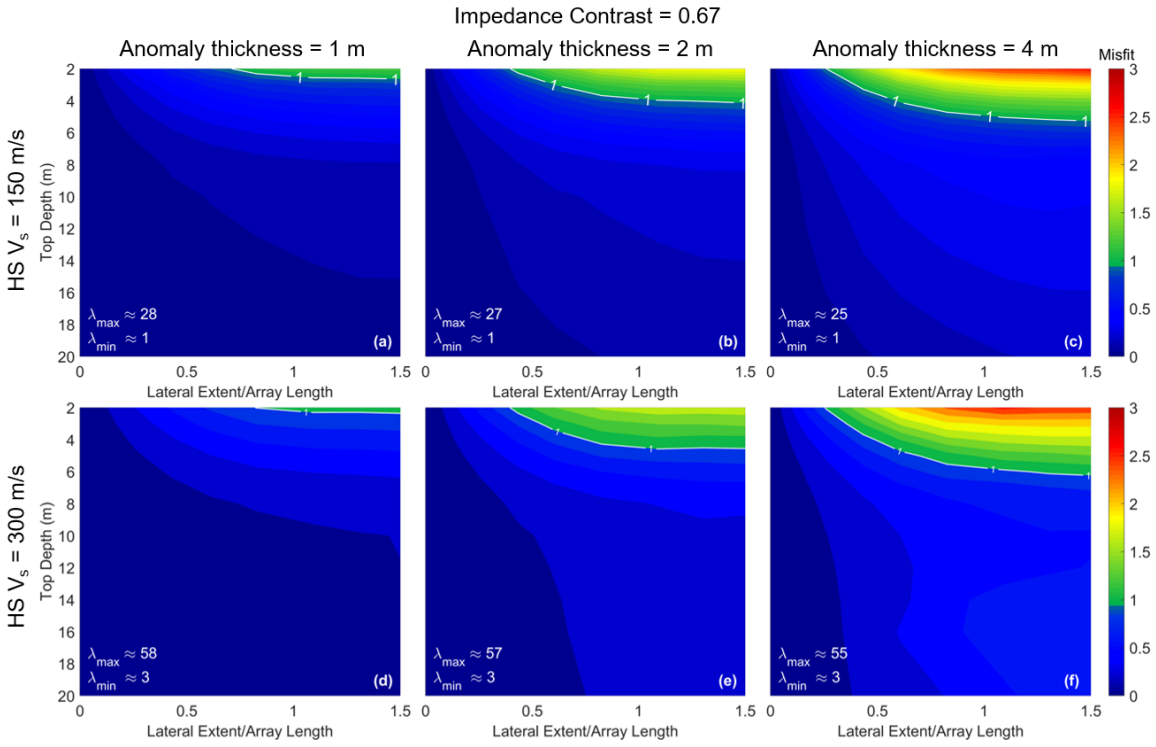

Figure 2.5: Summary plots of misfit values for an impedance contrast of 0.67. While all figures represent the same impedance contrast, (a-c) are for models containing a half-space with V_s equal to 150 m/s while (d-f) are for a half-space V_s of 300 m/s. Each row is listed in order of increasing anomaly thickness, such that (a-c) and (d-f) are for anomalies that are 1 m, 2 m, and 4 m thick, respectively. From these figures, it can be deduced that as an anomaly increases in thickness, the likelihood of detecting it increases (as indicated by higher misfit values with warmer colors). Additionally, the maximum depth at which an anomaly may be detected increases as the thickness increases. For higher half-space V_s values (d-f), longer wavelengths may be measured relative to lower V_s values (a-c), resulting in a higher chance of detecting anomalies at depth.

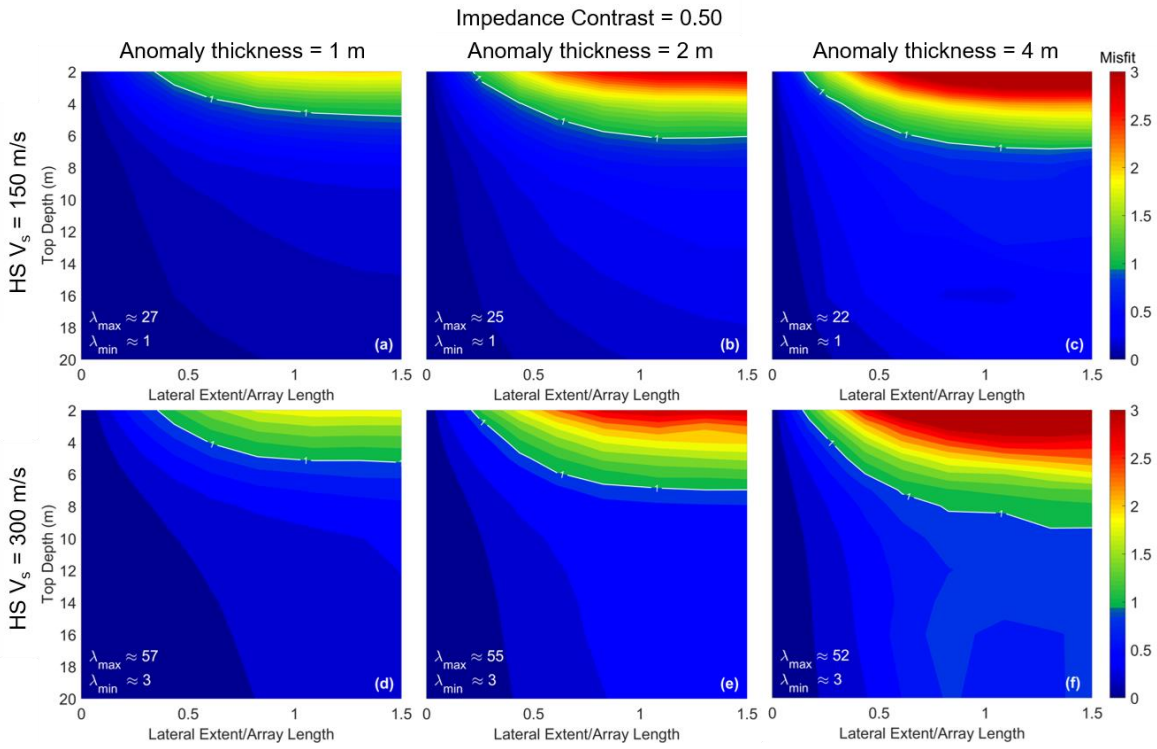

Figure 2.6: Summary plots of misfit values for an impedance contrast of 0.50. While all figures represent the same impedance contrast, (a-c) are for models containing a half-space with Vs equal to 150 m/s while (d-f) are for a half-space Vs of 300 m/s. Each row is listed in order of increasing anomaly thickness, such that (a-c) and (d-f) are for anomalies that are 1 m, 2 m, and 4 m thick, respectively. These figures show a marked difference from Fig. 5 in that across all models, anomalies in general are more likely to be detected given a higher impedance contrast between an anomaly and surrounding soil. In particular, the top depth at which a 1 m-thick anomaly may be detected has nearly doubled, and the likelihood of detecting 2 m- and 4 m-thick anomalies has significantly increased for similar depths.

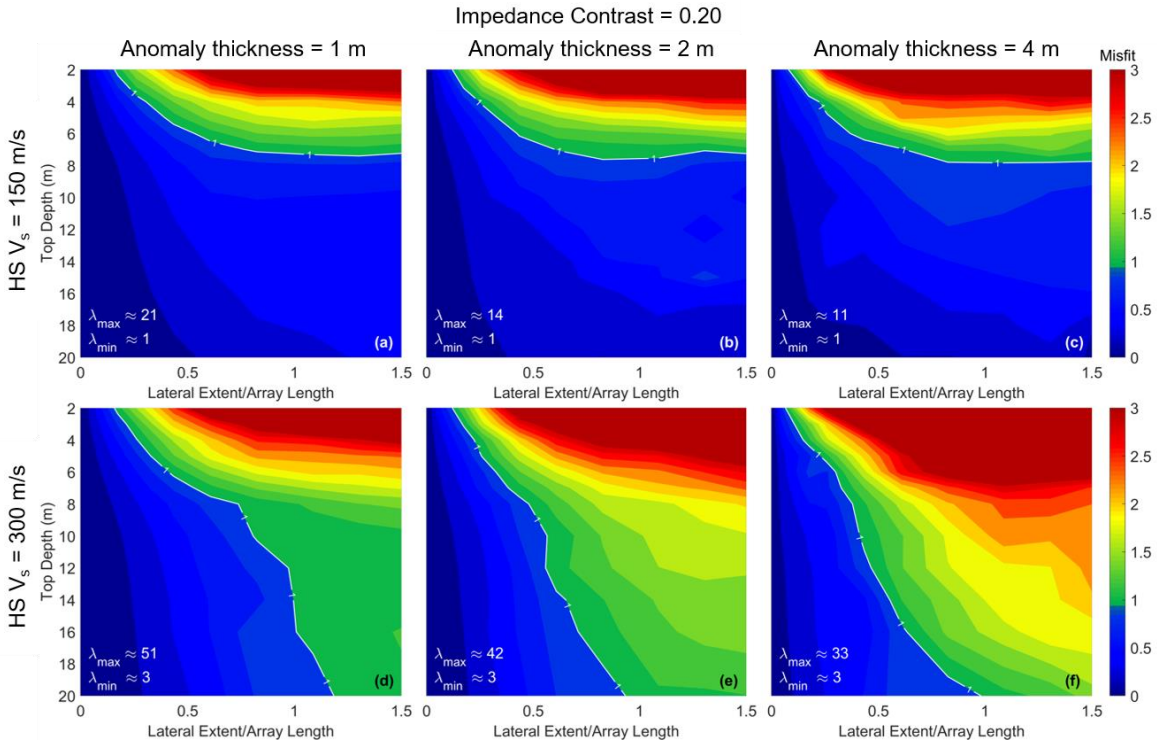

Figure 2.7: Summary plots of misfit values for an impedance contrast of 0.20. While all figures represent the same impedance contrast, (a-c) are for models containing a half-space with V_s equal to 150 m/s while (d-f) are for a half-space V_s of 300 m/s. Each row is listed in order of increasing anomaly thickness, such that (a-c) and (d-f) are for anomalies that are 1 m, 2 m, and 4 m thick, respectively. Note that these figures vary significantly compared to Fig. 2.5 and Fig 2.6. Specifically, (d-f) show that for an anomaly that is roughly the same length or longer than an array, the likelihood of detecting it is still possible even at relatively large depths. This is likely due to the high impedance contrast providing data for treatment models that are easily distinguishable from that of the control models as many dispersion curves exhibited higher modes.

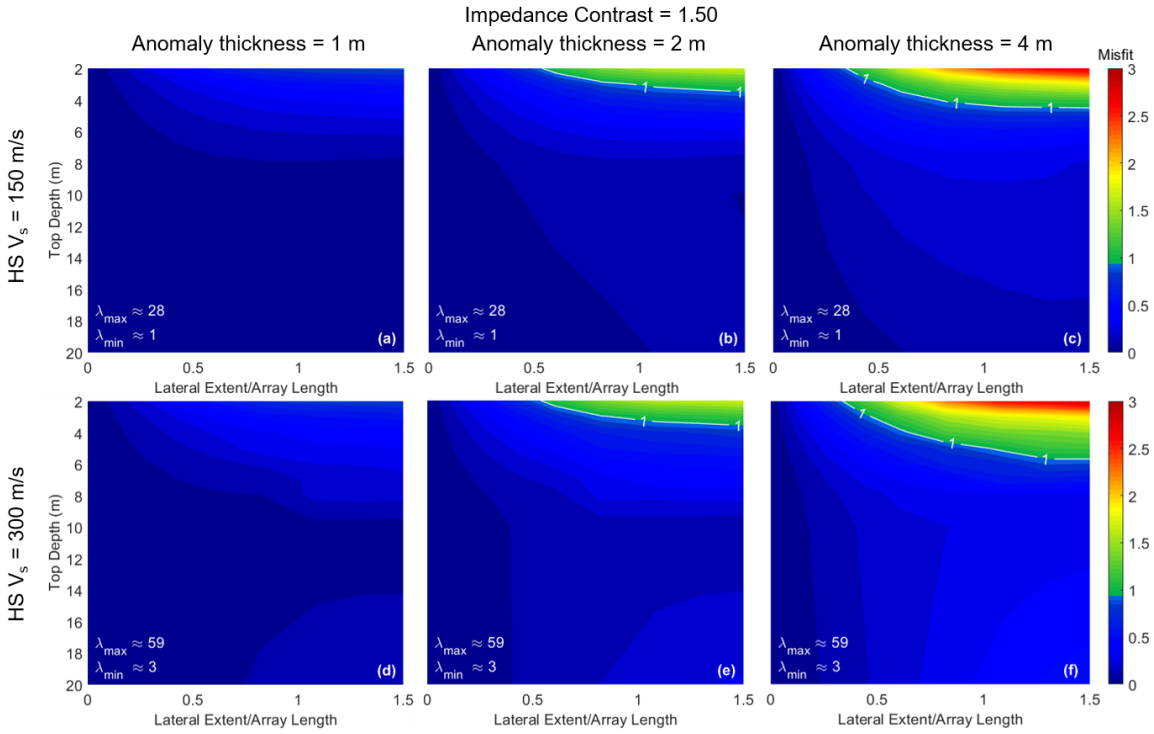

Figure 2.8: Summary plots of misfit values for an impedance contrast of 1.5. While all figures represent the same impedance contrast, (a-c) are for models containing a half-space with Vs equal to 150 m/s while (d-f) are for a half-space Vs of 300 m/s. Each row is listed in order of increasing anomaly thickness, such that (a-c) and (d-f) are for anomalies that are 1 m, 2 m, and 4 m thick, respectively. These models are similar to those presented in Fig. 5; however, these models contain anomalies that are stiffer than the surrounding material. Although it is difficult to detect 1 m-thick anomalies, the possibility of detection increases as the thickness of the anomaly increases, similar to previously discussed trends. Additionally, when compared to Fig. 5, stiffer anomalies are shown to be more difficult to detect than softer anomalies.

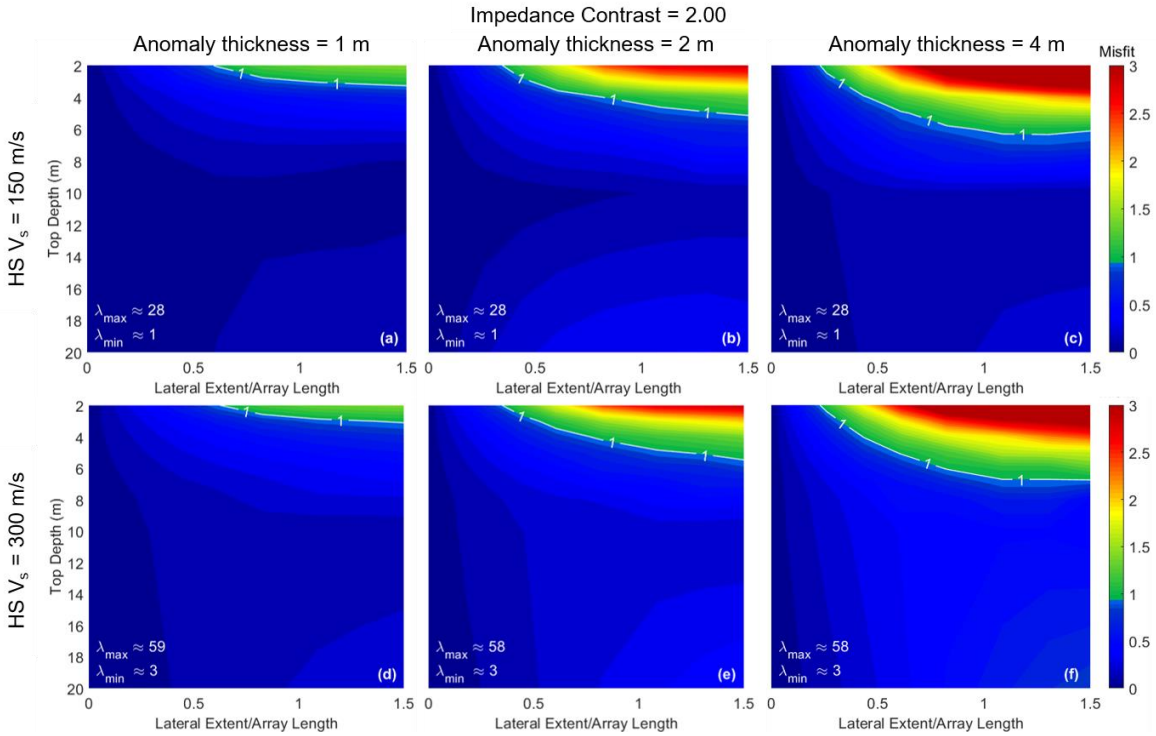

Figure 2.9: Summary plots of misfit values for an impedance contrast of 2.0. While all figures represent the same impedance contrast, (a-c) are for models containing a half-space with Vs equal to 150 m/s while (d-f) are for a half-space Vs of 300 m/s. Each row is listed in order of increasing anomaly thickness, such that (a-c) and (d-f) are for anomalies that are 1 m, 2 m, and 4 m thick, respectively. Addition-ally, these models contain anomalies that are stiffer than the surrounding material. Compared to an impedance contrast of 1.5, these plots show that a larger impedance contrast results in higher detection of anomalies. As thickness increases, the lower bound of detectability also increases, similar to Fig. 6.

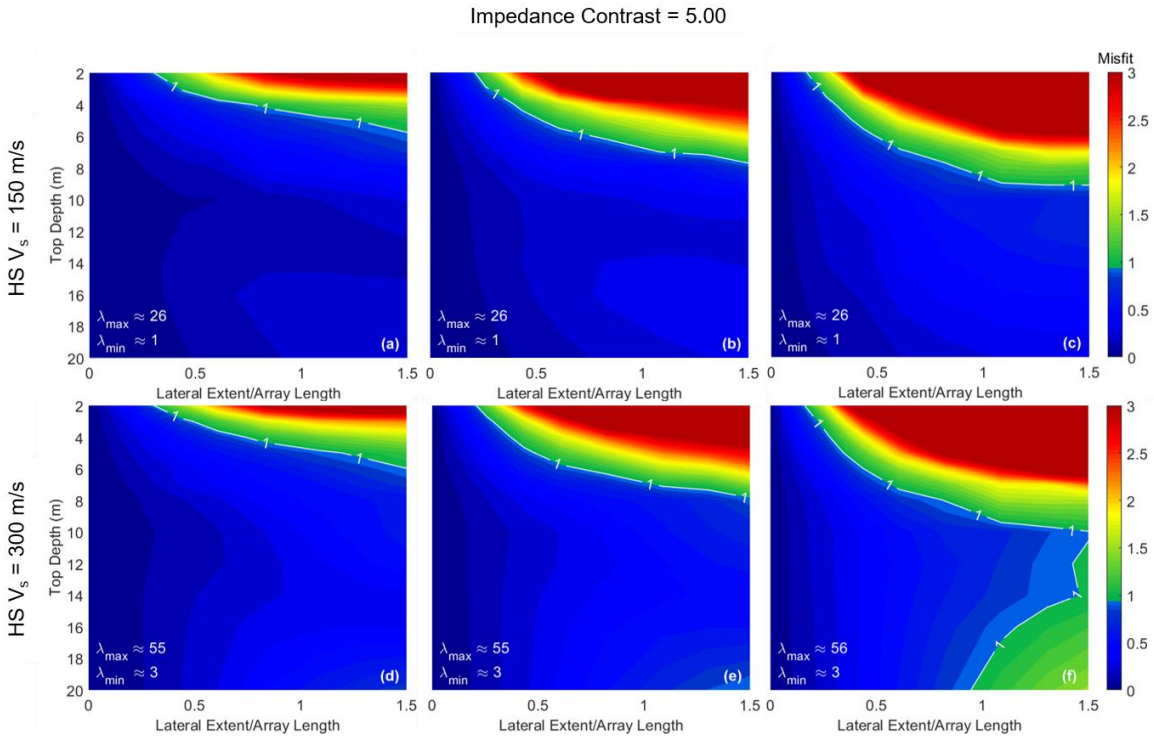

Figure 2.10: Summary plots of misfit values for an impedance contrast of 5.0. While all figures represent the same impedance contrast, (a-c) are for models containing a half-space with V_s equal to 150 m/s while (d-f) are for a half-space V_s of 300 m/s. Each row is listed in order of increasing anomaly thickness, such that (a-c) and (d-f) are for anomalies that are 1 m, 2 m, and 4 m thick, respectively. Additionally, these models contain an anomaly that is stiffer than the surrounding material. It should be noted that these models provided erratic data at higher depths. Particularly, models containing a 4 m-thick anomaly in soil with a V_s of 300 m/s exhibited dispersion data that cannot "see" through an anomaly, which resulted in higher misfits than otherwise expected. Therefore, results below roughly 10 to 12 m are not considered to be trustworthy.

Table 2.3: Summary of results for all models

Imp. Contrast	Half-space V_s (m/s)	Anomaly Thickness (m)	Max. Likely Detectable Depth (m)	Min. Likely Detectable Size Relative to Array	Min. Likely Detectable Lateral Extent (m)
0.67	150	1	3	0.70	16
		2	4	0.40	9
		4	5.5	0.25	6
	300	1	2.5	0.80	18
		2	4.5	0.40	9
		4	6	0.25	6
0.50	150	1	5	0.35	8
		2	6	0.23	5
		4	7	0.15	3.5
	300	1	5.5	0.35	8
		2	7	0.21	5
		4	9.5	0.15	3.5
0.20	150	1	7[1]	0.15	3.5
		2	7[1]	0.13	3
		4	7.5[1]	0.08	2
	300	1	+20[2]	0.15	3.5
		2	+20[2]	0.12	3
		4	+20[2]	0.08	2
1.5	150	1	-	-	-
		2	3.5	0.55	12.5
		4	4.5	0.35	8
	300	1	-	-	-
		2	3.5	0.55	12.5
		4	6	0.35	8
2.0	150	1	3	0.60	14
		2	5	0.35	8
		4	6	0.25	6
	300	1	3	0.63	14.5
		2	5.5	0.35	8
		4	7	0.23	5
5.0	150	1	5.5	0.30	7
		2	7.5	0.20	4.5
		4	9	0.18	4
	300	1	6	0.30	7
		2	8	0.20	4.5
		4	10[3]	0.15	3.5

1. Although it was expected that increases in thickness would result in increases in maximum detectable depth, these data showed unusual trends. Specifically, measured wavelengths were shown to decrease with changes in thickness, as further described in Sec. 2.4.
2. The depths of detection for these models extended beyond the maximum depth of 20 m used in this study. This was due to the presence of significant higher modes, which resulted in large misfit values for each set of models that resulted in no visible lower bound for a misfit of 1.0.
3. It was expected that a 4 m-thick anomaly would show an increase in maximum detectable depth for this impedance contrast and half-space Vs pairing. However, the dispersion trends showed that as the depth to the anomaly increased, the chance to "see" through the anomaly decreased, which led to increases in misfit as further described in Sec. 2.4.

When examining Fig. 10, which represents models with an impedance contrast of 5.0, it is clear that the results for models generated with a half-space Vs of 300 m/s differ significantly at deeper depths compared to those generated with a Vs of 150 m/s. In particular, models containing a 4 m-thick anomaly (Fig. 2.10f) show that the potential to detect an anomaly actually in-creases for depths below 16 m. This unexpected change in misfit can be explained with careful consideration of the dispersion data. For an anomaly placed at various depths, with all other variables held constant, there are four stages of note. First, the anomaly is near the sur-face and can easily be detected (i.e., has a high misfit). Second, the anomaly moves deeper and although it is still being "seen" by the surface wave, its velocity is being averaged with the material above and below it and is therefore less easily detected (i.e., has a relatively lower misfit). Third, the anomaly approaches the bot-tom-most range that the surface wave can "see", and since it is in effect no longer being averaged with a material of a different velocity below it, the anomaly ap-pears to be easier to detect (i.e., misfit begins to in-crease). Fourth, the top of the anomaly is below the maximum detectable depth and therefore cannot be detected (i.e., misfit is approximately 0). This trend is il-lustrated in Fig. 2.11 using anomalies represented in Fig. 2.10f for a lateral extent of 36 m with increasing top depths of 2, 14, and 20 m. Specifically, the first

three stages are shown. When the depth of the anomaly in-creases from 2 to 14 m, the misfit value is shown to de-crease significantly from 12.6 to 1.0. However, when the depth of the anomaly increases to 20 m, the misfit slightly increases to 1.6. The fourth stage in which the anomaly is no longer detected, i.e., when the misfit approaches zero, is not shown as this stage extended be-yond the depths used in this study. For each of the conditions considered, all four stages may or may not be clearly present, although this lends a physical explanation of the data in regard to the contour plots presented herein.

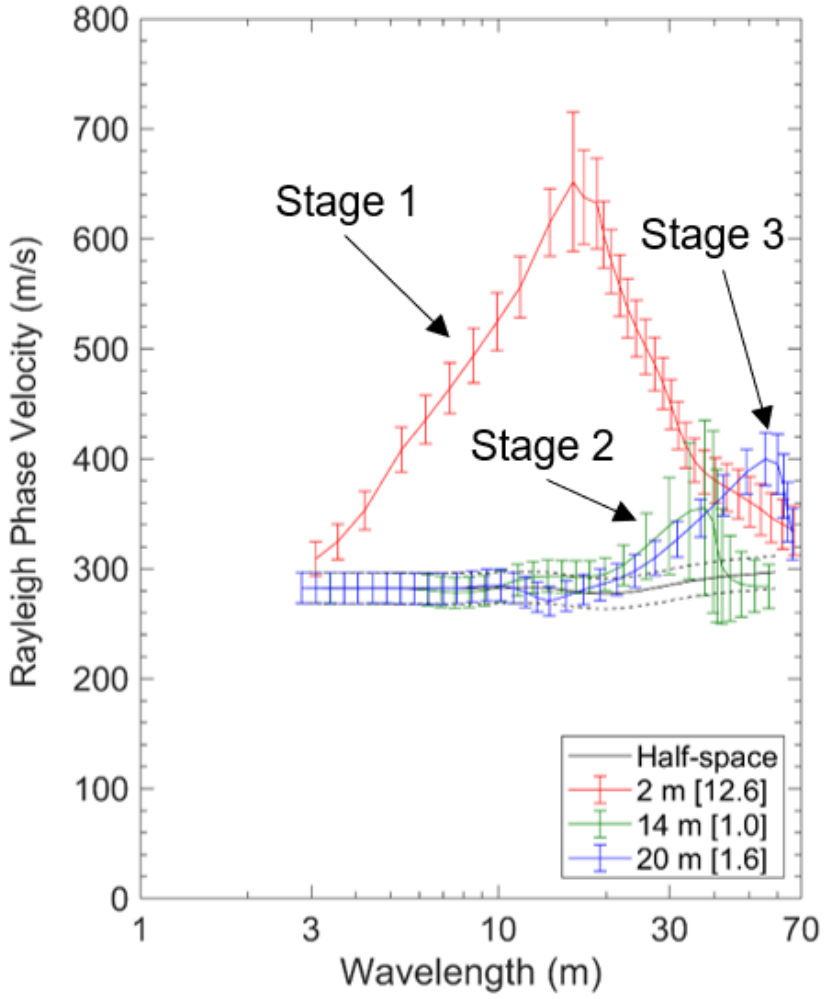

Figure 2.11: Three stages of detectability are shown for an anomaly that is 4 m-thick, 36 m wide, and with increasing top depths of 2, 14, and 20 m, which are indicative of the trends shown in Fig. 10f. Stage 1 shows that the anomaly is easily detectable, as indicated by the high misfit of 12.6. As the anomaly is placed deeper (stage 2), its velocity begins to be averaged with the surrounding soil, leading to a lower misfit of 1.0. Once the anomaly is placed at relatively larger depths (stage 3), surfaces waves can no longer "see" through the anomaly and the dispersion data do not return to the theoretical half-space velocity as expected, which leads to higher misfits. Stage 4, in which this anomaly should no longer be detectable, is not shown as this stage occurs beyond 20 m, which was the maximum depth used in this study.

2.5 CONCLUSION

To address the limited literature available regarding the quantitative ability of the MASW method to detect subsurface anomalies, typical testing procedures were simulated using synthetic control (i.e., without an anomaly) and treatment (i.e., with an anomaly) models. The misfit between the dispersion data of the control and treatment models were summarized quantitatively and used to illustrate whether a particular anomaly could or could not likely be detected. To allow for practical usage of this study, the quantitative misfit values were used to create example feasibility plots such that the likelihood of detecting an anomaly of a given geometry can be assessed prior to performing the field acquisition.

In short, the results presented in Fig. 2.5-10 and Table 2.3 reveal that the ability to detect an anomaly is largely dependent on its impedance contrast with the surrounding material and to a lesser extent on its size. In particular, lower impedance contrasts (soft anomalies) allow for greater chances of detection when compared to higher impedance contrasts (stiff-er anomalies). Furthermore, a site with higher velocities leads to greater chances for detection of anomalies at depth compared to a site containing soils with low velocities due to an increase in the measured wavelengths, provided the frequency range measured at both sites is consistent. At impedance contrasts greater than 1.0, an anomaly must be roughly half the length of the array used during testing to likely be detected, whereas at an impedance contrast less than 1.0, the anomaly may be as small as a quarter of the array length. As expected, the results show that as the thickness of an anomaly increases, the potential to detect it increases, while an increase in depth to the top of the same anomaly results in a decrease in its detectability. It should be noted again that while a misfit of 1.0 was used as a general guideline for the boundary of easy/likely detection in this study, mis-fits below 1.0 do not strictly indicate that an anomaly will not be detected;

rather, the authors have interpreted a misfit below 1.0 to indicate that these anomalies will be more difficult, or in general less likely, to be detected given typical levels of experimental dispersion data uncertainty.

Although this study emphasized the importance of detecting anomalies when performing site characterization, the ability to accurately resolve irregular velocity profiles through inversion is similarly significant. The authors acknowledge that detecting an anomaly is present does not necessarily mean that the anomaly may be resolved in terms of its shape and velocity. Although we hope this work may be useful to others planning site characterization studies using 2D MASW for anomaly detection, further work is needed to determine the potential for resolving an anomaly's shape, stiffness, and location given that it can likely be detected based on its dispersion signature.

2.6 Acknowledgements

This material is based upon work supported by the National Science Foundation Graduate Research Fellowship Program under Grant No. DGE – 1610403. Any opinions, findings, and conclusions or recommendations expressed in this material are those of the authors and do not necessarily reflect the views of the National Science Foundation.

Additionally, the authors would like to thank the Texas Advanced Computing Center (TACC) for providing access to the high-performance computing resource Stampede2, which was invaluable for completing this study. The authors would also like to express gratitude towards the creators of DENISE for releasing their code as an open-source project, which proved to be the foundation for this study.

Chapter 3: Ability of the MASW Method Resolve Subsurface Anomalies

This chapter contains a conference paper manuscript that has been accepted for publication at the International Foundations Conference and Equipment Expo in Dallas, TX, USA on 10-14 May 2021. The full citation is listed below:

Ugur, A., Crocker, A. J., Vantassel, J., & Cox, B. (2021). Ability of the multichannel analysis of surface waves method to resolve subsurface anomalies. Accepted to the International Foundations Conference and Equipment Expo in Dallas, TX, USA on 10-14 May 2021.

As first author, I was responsible for approximately 20% of the project planning, 50% of the data acquisition, 100% of the data processing, and 50% of the results interpretation.

ABSTRACT

This study examines the ability of the multichannel analysis of surface waves (MASW) method to accurately recover the size, stiffness, and depth of subsurface anomalies. The dispersion data considered in this paper were derived from waveforms generated using two-dimensional (2D) finite-difference elastic wave-propagation simulations. These simulations were performed to replicate a typical MASW field experiment on models with and without subsurface anomalies, referred to as "treatment" and "control" models, respectively. In a previously published study, the treatment and control models were compared exclusively based on differences between their experimental dispersion data to determine whether or not the anomaly could likely be detected. This study examines whether those models previously categorized as containing a detectable anomaly, based on their experimental dispersion data, can be inverted to accurately resolve the anomaly's size, stiffness, and depth. To rigorously perform the inversions, we adopt the procedures recommended by the surface wave inversion workflow SWinvert, which involves using multiple large-scale global-search inversions to address the problem's non-linearity and multiple layering parameterizations to address the problem's non-uniqueness. Following the inversion process, the shear wave velocity (Vs)

profiles from the single “best” model associated with each layering parameterization are compared to the 1D Vs profile from the centerline of the true model using an error function to quantitatively assess the ability of the MASW method to accurately resolve subsurface anomalies. Intuitively, the ability to resolve subsurface anomalies is shown to improve as the anomaly is moved closer to the ground surface and its lateral extent increases. Surprisingly, however, in this study anomalies with lateral extents less than approximately ½ the array length located at depths greater than 5 m most likely cannot be resolved accurately by using MASW, even when the anomalies are relatively thick (> 2 m) and the impedance contrasts are notably high (> 2).

3.1 INTRODUCTION

In-situ soil characterization with non-invasive surface wave methods has been widely used in past decades because they are relatively inexpensive and, perhaps erroneously presumed, easy to perform. Of these methods, the multichannel analysis of surface waves (MASW) method (Park et al. 1999; Foti 2000) is one of the most common. Although this method is typically used to develop one-dimensional (1D) subsurface shear wave velocity (Vs) profiles, an area of particular interest is the application of MASW for anomaly detection. Such applications include investigation of weak zones in levee systems (Rahimi et al. 2018), detection of karst conduits (Debeglia et al. 2006), detection of voids near the surface (i.e., < 3 m) (Nolan et al. 2011), shallow man-made tunnel detection (i.e., < 3 m) (Sloan et al. 2013), delineation of sink-holes, voids, and mines (Sloan* et al. 2015; Ivanov et al. 2016) identification of the location of a dam’s compacted core (Hock et al. 2007), and evaluation of unknown subsurface bridge foundations (Mahvelati and Coe 2017). The successful application of surface wave methods for anomaly detection relies on the anomaly being within the vertical and horizontal detection limits, which depend on a

number of factors, including: (a) the receiver spacing and length of the MASW array, (b) the minimum and maximum frequencies/wavelengths resolved during testing, (c) the size of the anomaly, and (d) the stiffness contrast of the anomaly relative to the surrounding materials (Xia et al. 1999; Park 2005; Ivanov et al. 2008). However, successful detection of an anomaly at the dispersion processing stage does not necessarily equal successful resolution of the anomaly during the inversion stage. Accurately resolving subsurface anomalies can be challenging for surface wave methods due to: (1) the 1D nature of the forward problem used to calculate theoretical dispersion curves from a trial subsurface model, whereas anomalies inherently induce 2D/3D variability in the subsurface, and (2) the non-uniqueness of surface wave inversion, which results in a number of candidate models that can fit the experimental data equally well.

In this paper, we consider synthetic subsurface models developed in a previous study by Crocker et al. (2020). The development of these models began with a simple uniform body of soil (half-space) containing no anomalies. These control models were developed with a constant mass density (ρ) and Poisson‘s ratio (ν) for Vs values of 150 and 300 m/s. Then, anomalies with various combinations of size (lateral extent and thickness), stiffness, and depth were placed into the control models to produce treatment models (refer to Figure 3.1a). These anomalies were created to be either softer or stiffer than the surrounding half-space using several different impedance contrasts (the ratio between the anomaly Vs to the half-space Vs). For example, a treatment model with an anomaly impedance contrast of 2.0 and a half-space with Vs equal to 150 m/s contains an anomaly with Vs equal to 300 m/s. Approximately 3,000 different treatment models were developed in this manner.

Following model development, Crocker et al. (2020) used a 2D finite-difference pro-gram (Köhn et al. 2012) to simulate wave propagations for MASW experiments at the

surface of models with and without anomalies. As shown in Figure 3.1a, several different shot locations were used for each model and the simulated waveforms were recorded using a 24-channel MASW array with 1-m spacing between receivers (total array length of 23 m). The simulated wavefields were then processed using the frequency domain beamformer method (Zywicki and Rix, 2005) to obtain dispersion data. The dispersion data from the treatment and control models were compared quantitatively using a dispersion misfit function (i.e., L1 norm of residuals between the mean treatment and control experimental dispersion data, normalized by the control model's uncertainty). The obtained misfit, which we will hereafter refer to unambiguously as the relative dispersion misfit (Mdc,rel), was then used to categorize anomalies as likely detect-able (i.e., Mdc,rel > 1) or likely non-detectable (i.e., Mdc,rel < 1). To provide a convenient reference, the results from similar models were synthesized into figures such as that shown in Figure 1b, which for a given impedance contrast (IC), anomaly thickness (T), and half-space velocity (Vs,hs), the user could assess the range of relative dispersion misfits as a function of the anomaly's lateral extent normalized by the MASW array length (LE/AL; abscissa) and the anomaly's top depth (ordinate). For example, Figure 1b shows Mdc,rel for models with IC = 5.0, T = 2 m, and Vs,hs = 150 m/s. As mentioned previously, a Mdc,rel value of 1.0 was considered as the boundary between models containing anomalies that were, and were not, likely detectable, and is indicated for reference with a thin white line in Figure 3.1b.

Due to the complexity and computational expense of surface wave inversion, through the course of this study, we inverted only 120 of the nearly 3,000 treatment models developed by Crocker et al. (2020). Models were selected to encompass various anomaly thicknesses, LE/AL ratios (noting that AL = 23 m was constant for all models discussed herein), depths, and impedance contrasts to observe the influence of each factor on anomaly resolution. We focused primarily on models that were likely detectable based on high

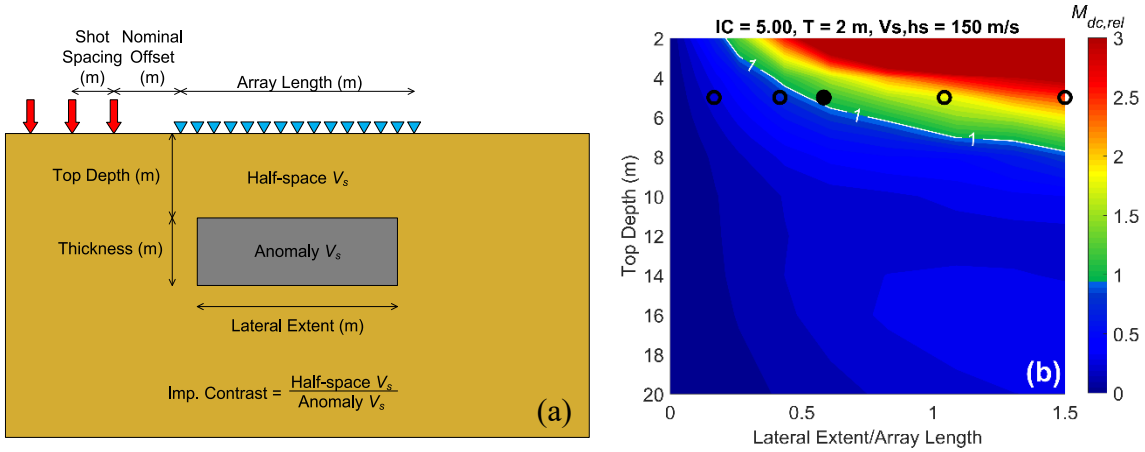

Figure 3.1: (a) Schematic of a treatment model, and (b) summary of relative dispersion misfits (Mdc,rel) from Crocker et al. (2020) for treatment models with an impendence contrast (IC) of 5, thickness (T) of 2 m, and half-space shear wave velocity (Vs,hs) of 150 m/s. Black circles at a top depth of 5 m indicate the treatment models selected for inversion to explore the effect of the anomalies' lateral extent/array length (LE/AL) ratio.

Mdc,rel (i.e., > 1), and there-fore the most likely to be resolvable, however, some models with low Mdc,rel (i.e., < 1) were also inverted to verify this assumption. To synthesize the most interesting results of the inversion study, this paper will only focus on two model trends. The first trend involves treatment models with increasing LE/AL ratios and constant thickness, depth, half-space velocity, and impedance contrast (such as those indicated by black circles in Figure 3.1b). The second trend involves treatment models with increasing depth to the top of the anomaly and constant LE/AR ratios, thickness, half-space velocity, and impedance contrast.

3.2 Inversion Methodology

Before discussing the details of our inversion methodology, we offer a brief summary of surface wave inversion. The purpose of surface wave inversion is to find the 1D subsurface model(s) with layer thicknesses (H), Vs, compression wave velocity (Vp),

and mass density (ρ) whose solution to the analytical forward problem (i.e., theoretical dispersion curve) best matches the experimental dispersion data. Of particular importance is the determination of the subsurface Vs profile, as it has the greatest sensitivity in the forward problem and importance in engineering practice. To assess the goodness-of-fit between a potential model's theoretical dispersion curve, as calculated through the forward problem (Thomson 1950; Haskell 1953), and the experimental dispersion data, inversion requires the definition of a dispersion misfit (Mdisp). Mdisp is most typically a L2 norm of error, or some normalized version thereof. In order to minimize Mdisp (i.e., find the best match between a candidate model's theoretical dispersion curve and the experimental dispersion data), various inversion algorithms have been proposed to alter the model properties. Once a model has been found whose theoretical dispersion curve closely matches the experimental dispersion data, it can be inferred that the model, and most importantly its Vs profile, is an acceptable representation of the subsurface. However, this process is not unique.

To rigorously invert the 120 sets of experimental dispersion data selected from Crocker et al. (2020), we adopt the surface wave inversion workflow SWinvert, developed by Vantassel and Cox (2020). This workflow entails using multiple large-scale global-search inversions to address the inverse problem's non-linearity and multiple parameterizations to consider non-uniqueness in the subsurface layering. The implementation details of this workflow are explained in the following sections.

3.3 Inversion Tuning Parameters

The inversions in this study were performed using the open-source tool SWbatch (Vantassel et al., 2020), which enables users to perform batch-style surface wave inversions that consider multiple trials to explore the inverse problem's non-linearity, and multiple

layering parameterizations to explore its non-uniqueness, as required by the SWinvert workflow. Since these in-versions can become computationally expensive, SWbatch has been developed into an easy-to-use web-application on the DesignSafe-CI (Rathje et al. 2017) workspace to allow users with no knowledge of high-performance computing to gain its benefits in their research. SWbatch is built upon the global-search Neighborhood Algorithm developed by Sambridge (1999) and implemented for surface-wave inversion in the Dinver module (Wathelet et al. 2004) of the open-source software Geopsy (Wathelet et al. 2020).

We invert each set of experimental dispersion data from the 120 treatment models considered using five different layering parameterizations (discussed next), each with five different inversion trials. For each trial inversion, we search 150,000 models, such that we consider 750,000 models in total for each layering parameterization (i.e., 150,000 models per trial and 5 trials per parameterization). To select a single answer for comparison with the true solution, we select the "best" (i.e., lowest misfit) model out of the 750,000 models for each layering parameterization. Because using such a large number of trial models is computationally expensive, we reduce some of the computational expense by resampling the experimental dispersion data prior to inversion using 20-30 points in log-frequency space (Vantassel and Cox 2020).

3.4 INVERSION PARAMETERIZATION

Developing inversion parameterizations is a crucial part of the inversion process to obtain reliable results (Di Giulio et al. 2012; Brady R. Cox and Teague 2016). The range of the parameterization (e.g., upper and lower limit on Vs) must be broad enough to include the true model, but also relatively restricted such that reasonable results are produced and

needless time is not spent searching areas of the parameter space that do not contain the true model. As mentioned previously, the treatment and control models were developed to have a constant ρ and ν with variable Vs and layer thicknesses. As such, the focus in this study is the inversion parameterization of Vs and the number of trial layers. To consistently parameterize Vs across all treatment models considered, we select a range of twice the highest Vs and half of the lowest Vs based on the true model. For example, for an IC of 5.0 and a Vs,hs of 150 m/s, the Vs of the anomaly would be 750 m/s, and therefore the chosen Vs inversion parameterization range was set at 75 (= 0.5*150) to 1,500 (= 2*750) m/s. While knowledge of the true Vs profile is untenable in practice, as the true model is never known, we do so here to ensure the parameterization contains the true model and avoid the time consuming process of iteratively adjusting the inversion parameterization, as is typically required in practice. We do not apply any limitations on the change in Vs (and Vp, discussed later) between layers. Furthermore, we do not constrain the velocity of any given layer to be faster than the layer above it, thereby allowing for the detection of soft anomalies and/or the detection of soft layers below stiff anomalies. This general approach of enabling velocity reversals in all trial layers is common practice when inverting dispersion data to detect subsurface anomalies. To parameterize layer thicknesses, we utilize Layering by Number's (LN) of 3, 4, and 5 and fixed-thickness layers (FTL) of 10 and 20. The LN parameterization is discussed at length in Vantassel and Cox (2020), but for the edification of the reader a brief summary is provided here. An LN=5, for example, divides the subsurface in-to 5 layers, including the half-space. The minimum thickness of each layer is controlled by the minimum experimental dispersion data wavelength (λ) divided by 3, while the maximum pro-file depth is controlled by dividing the maximum experimental dispersion data λ by a depth factor (df), which is taken as 2 in this study to satisfy the recommendations of Foti et al. (2018). In contrast, the FTL

approach parameterizes a profile with a set number of layers of equal/fixed thickness. FTL=10, for example, includes 10 layers of equal thickness between the surface and the maximum profile depth, defined in the same manner as that for LN. Of note to the reader, both approaches are programmed in SWprepost (Vantassel 2020), an open-source Python package for surface-wave inversion pre- and post-processing, such that these (and other) parameterizations can be generated programmatically and exported directly to the .param format used by Dinver.

While not the primary focus of attention here, the parameterization of Vp and mass density also deserve a brief discussion. The range of Vp for all layers was defined as twice the Vs range (i.e., 150 to 3,000 m/s for the example discussed above), while the Vp layer thickness-es were defined using an LN=3, regardless of the Vs layering parameterization. Mass density was always held constant at the true density of 2,000 kg/m3. Poisson's ratio, while not a true inversion parameter (as it is uniquely determined by Vs and Vp), is used by Dinver as an additional constraint available to the user to ensure the consistency of the Vs and Vp during inversion. Poisson's ratio was parameterized with an LN=1 and allowed to vary between 0.15 and 0.5.

To ensure reasonable results and expedite convergence to a good solution, the parameter ranges for both Vp and Vs were adjusted for the near-surface layers by interpreting the experimental dispersion data on a case-by-case basis. To illustrate the parameterization adjustment procedure, Figure 3.2a shows the experimental dispersion data from one treatment model in terms of frequency. The phase velocity is observed to be nearly constant at approximately 140 m/s between 30 to 100 Hz, which corresponds to wavelengths between 1 and 5 m ($\lambda=V/f$). Because the resolution depth can be approximated as λ/df, where df is 2 or 3, we can assert that a uniform soil layer exists between 2 to 3 m.

This allows us to then narrow the default velocity parameterization range in the upper 2 to 3 m from 75-1,500 m/s to a more reasonable, but still quite conservative, 75-250 m/s.

3.5 A Detailed Presentation of a Single Example

Before presenting the full results, we first discuss a single example to illustrate a few important points. Figure 3.2a shows the experimental dispersion data for the example treatment model in terms of frequency. The example model is composed of a Vs,hs of 150 m/s and an anomaly with a T of 2 m, LE/AL = 0.61 (i.e., LE = 14 m), top depth of 5 m, and Vs of 750 m/s (i.e., IC=5). As noted above, this model is indicated in Figure 3.1b by the solid black symbol, which has a relative dispersion misfit greater than 1 (meaning it is likely detectable). The 1D Vs pro-file at the middle of the treatment model is shown as the solution in Figure 3.2b. Figure 3.2a also shows the single "best"/lowest misfit theoretical dispersion curves from each of the five considered inversion parameterizations. Qualitatively, the theoretical dispersion curves are all observed to fit the experimental data extremely well across all frequencies. This qualitative assessment is confirmed quantitatively by the low dispersion misfit values (Mdisp < 0.25), indicating an excellent fit between the theoretical dispersion curves and the experimental dispersion data. However, Figure 3.2b shows that the Vs profiles corresponding to these theoretical dispersion curves, which match the experimental dispersion data so precisely, poorly capture the anomaly's thickness and velocity, despite the LN parameterizations doing a fair job of capturing the anomaly's top depth. To assess the agreement between the true solution (i.e., the 1D Vs profile at the center of the model) and the best 1D Vs profile determined during inversion, and to further compare the best 1D Vs profiles obtained from different layering parameterizations, we calculate the model's Vs misfit (MVs) using the normalized L1 of residuals, proposed by Vantassel and Cox (2020). MVs is described in Equation 3.1:

$$M_{Vs} = \frac{1}{N}\sum_{i=1}^{N} \frac{|Vs_{i,inversion} - Vs_{i,solution}|}{Vs_{i,solution}} \quad (3.1)$$

where N is the total number of depth discretizations, $Vs_{i,inversion}$ is the Vs of the best inversion result at depth i, and $Vs_{i,solution}$ is the Vs of the solution model at depth i. For this study, 0.1 m intervals were used to discretize the profiles from 0 to 20 m depth. The MVs values for the profiles shown in Figure 3.2b illustrate quantitatively that the LN parameterizations (MVs between 0.19 and 0.39) well outperform their FTL counterparts (MVs between 1.33 and 2.8), resulting in better estimates of the site's subsurface. However, this is not to imply that the LN parameterizations do a "good" job resolving the anomaly, as none of the parameterizations are able to capture both the anomaly's thickness and velocity. This comparison does, however, indicate that parameterizing an inversion using a large number of thin layers does not guarantee better resolution of subsurface anomalies (a common misconception) and is more likely to introduce spurious subsurface layering despite fitting the experimental dispersion data quite well (e.g., FTL=10).

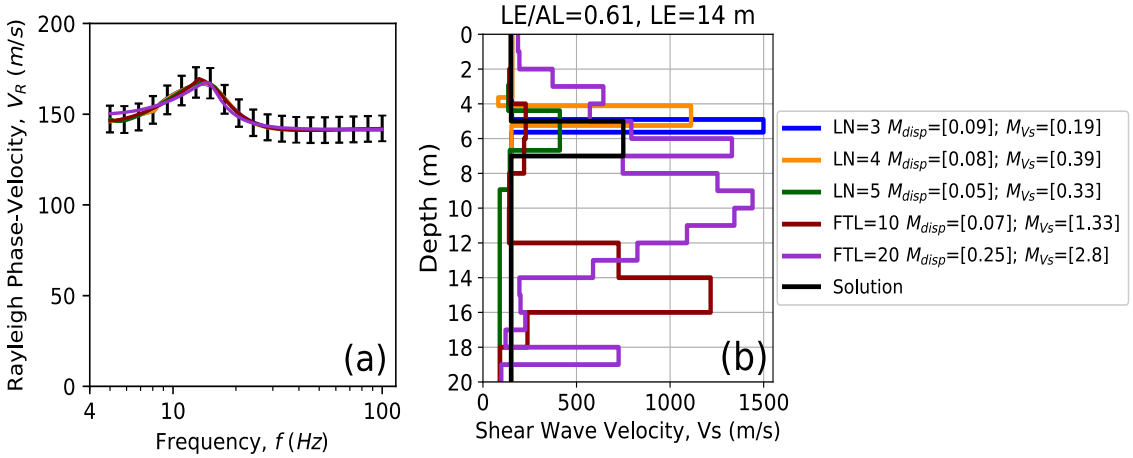

Figure 3.2: Experimental dispersion data in terms of (a) frequency for a treatment model with a half-space velocity (Vs,hs) of 150 m/s and an anomaly with a thickness (T) of 2 m, lateral extent of 14 m (i.e., LE/AL = 0.61), top depth of 5 m, and velocity of 750 m/s (i.e., IC=5). The Vs profiles resulting from the inversion of experimental dispersion data in panel (a) are shown in panel (b). Misfit values between theoretical and experimental dispersion data (Mdisp) and between inverted and true solution Vs profiles (MVs) for each LN and FTL parameterization are indicated in the legend.

3.6 Discussion of Many Inversion Results

We now present the inversion results pertaining to the two categories of interest for this paper, which include the effects of: (1) increasing anomaly lateral extent, and (2) increasing top depth to the anomaly. We begin with the effect of increasing lateral extent. Figure 3.3 summarizes the inversion results for a model with Vs,hs of 150 m/s and an anomaly with a T of 2 m, top depth of 5 m, Vs of 750 m/s, and five different LE/AL ratios. Figure 3a illustrates that the Mdc,rel for the five lateral extents (black circles) increases from approximately 0.3 (unlikely detectable) at LE/AL = 0.17 (4 m LE) to 2.5 (likely detectable) at LE/AL = 1.56 (36 m LE). We now assess whether these anomalies can be accurately resolved using MASW inversions. Figures 3.3b-f show the inversion results for increasing LE/AL ratios. We observe qualitatively (i.e., visually assessing the Vs profiles)

and quantitatively (i.e., comparing MVs) that as the lateral extent in-creases [i.e., proceed from (b) to (f)], the quality of the Vs resolution for the reasonable parameterizations (i.e., LN) generally improves. However, it is important to note that this improvement is not monotonic with increasing LE/AL ratio (due to a number of complicating factors discussed later), but only a general improving trend from poor resolution at LE/AL = 0.17 (Figure 3.3b) to better resolution at LE/AL = 1.56 (Figure 3.3f). Importantly, while we note that the anomaly resolution improves with increasing lateral extent, this is not to say that any of the anomalies (even the one with the largest lateral extent) is well-resolved, but rather that anomalies with limited lateral extent are much less well-resolved. From this set of examples, we conclude that the MASW method is unlikely to accurately resolve subsurface anomalies when they have small LE/AL ratios (less than ~ 0.5), even when the anomalies are located relatively close to the ground surface (top depth of 5 m) and are relatively thick (2 m). Furthermore, for anomalies with LE/AL > 0.5 MASW is better able to resolve the anomaly's thickness and top depth, but remains unable to reliably resolve the anomaly's velocity.

We now examine the effect of increasing anomaly top depth, or moving the anomaly deeper into the control model. Figure 3.4 summarizes the inversion results for a model with a Vs,hs of 300 m/s and an anomaly with a T of 4 m, LE/AL ratio of 0.61, Vs of 600 m/s (i.e., IC=2), and five different top depths. Figure 3.4a from Crocker et al. (2020) illustrates that the Mdc,rel for the five models (black circles) decrease from 2.8 (likely detectable) at 2 m top depth to 0.4 (unlikely detectable) at 10 m top depth. The inversion results used to investigate anomaly top depths of 2, 4, 5, 8, and 10 m are presented in Figures 4b-f. A comparison of the results confirms that the ability to resolve an anomaly deteriorates as its depth increases. However, the results follow a less clear and consistent pattern due to the compounding impact of the lateral extent, which at 14 m is just slightly

above the LE/AL > 0.5 threshold for likely anomaly resolution, as dis-cussed previously. Yet, despite these complicating factors, we observe that for those anomalies closer to the surface (top depth < 5 m), the reasonable parameterizations (i.e., LNs) are generally able to recover the anomaly's top depth, although they are unable to consistently recover its thickness and velocity. Whereas those models with deeper anomalies (top depth > 5 m) are un-able to even recover the anomaly's top depth. From this example, we observe that the ability to resolve a subsurface anomaly decreases as its top depth increases, as anticipated. In particular, we find for this example with a lower IC, that the MASW method is unable to accurately resolve the thickness and velocity of the anomaly at any top depth, despite the anomaly being of considerable size (4 m thick and 14 m lateral extent).

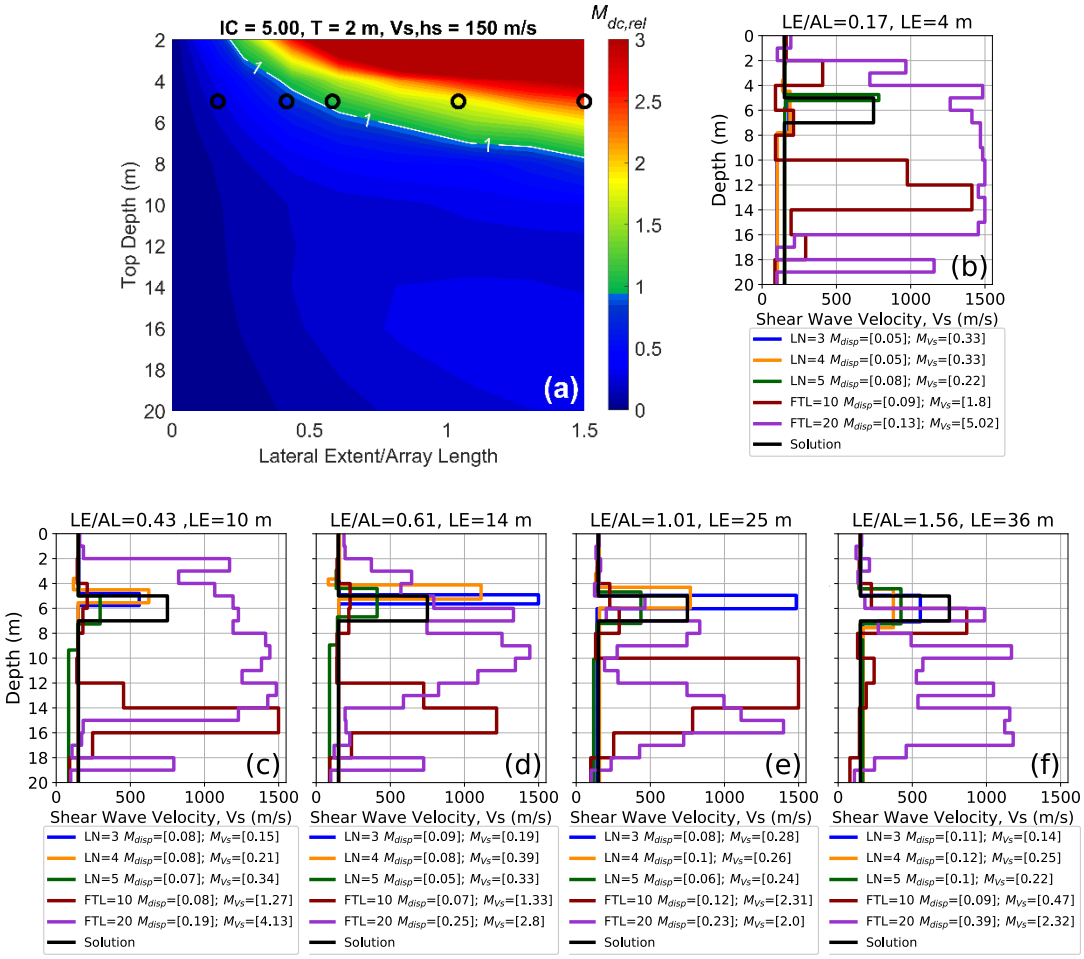

Figure 3.3: (a) Summary of relative dispersion misfit (Mdc,rel) for a model with half-space velocity (Vs,hs) of 150 m/s and an anomaly with a thickness of 2 m, top depth of 5 m, Vs of 750 m/s (IC=5), and five different LE/AL ratios. (b) – (f) present the inversion results for models with anomalies with lateral extents equal to 4, 10, 14, 25, and 36 m, respectively. These models are further indicated by black circles on Figure 3.3a. Misfit values between theoretical and experimental dispersion data (Mdisp) and between inverted and true solution Vs profiles (MVs) for each LN and FTL parameterization are indicated in the legend.

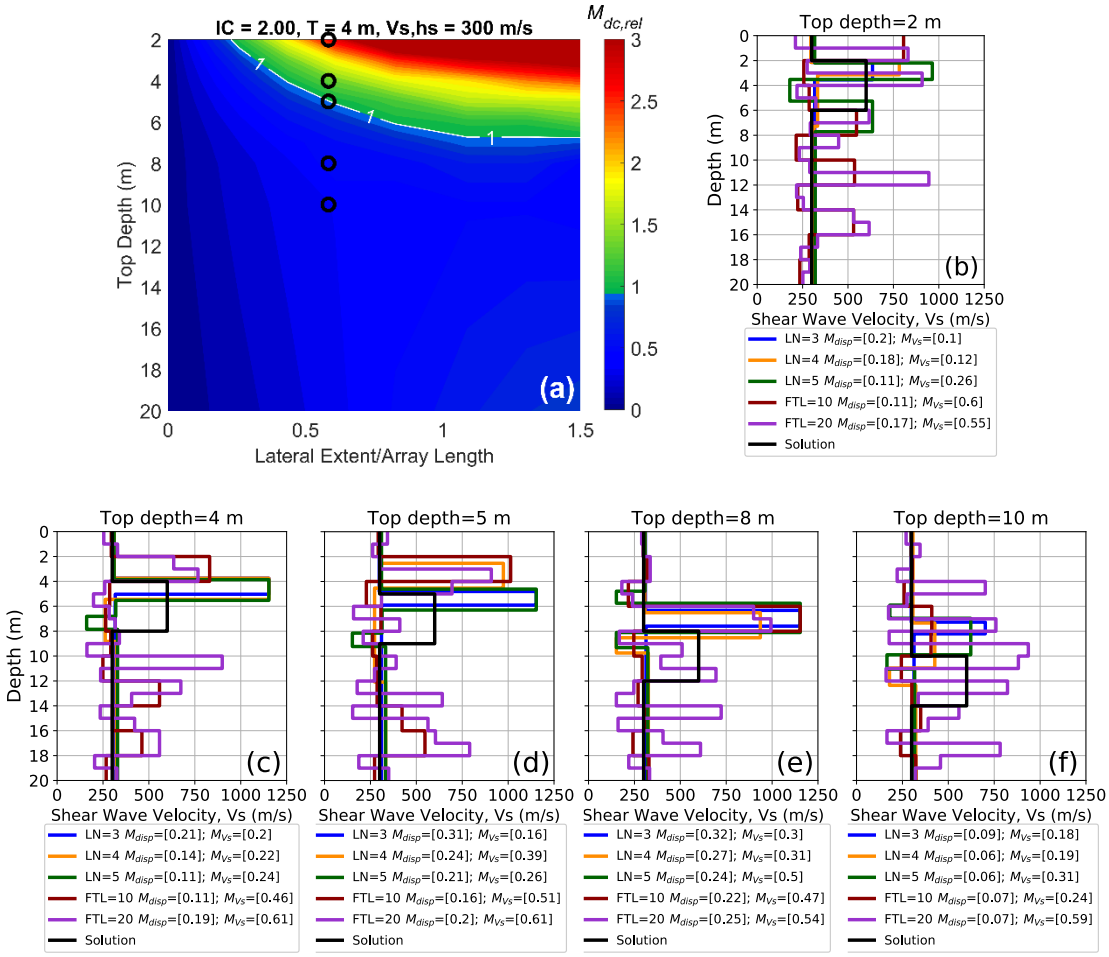

Figure 3.4: (a) Summary of relative dispersion misfit (Mdc,rel) for a model with half-space velocity (Vs,hs) of 300 m/s and an anomaly with a thickness of 4 m, Vs of 600 m/s (IC=2), lateral extent of 14 m (i.e., LE/AL = 0.61), and five different top depths. (b) – (f) present the inversion results for models with anomalies with top depths equal to 2, 4, 5, 8, and 10 m, respectively. These models are further indicated by black circles in panel (a). Misfit values between theoretical and experimental dispersion data (Mdisp) and between inverted and true solution Vs profiles (MVs) for each LN and FTL parameterization are indicated in the legend.

3.7 CONCLUSION

This study examines the ability of the MASW method to accurately recover the size, stiffness, and depth of subsurface anomalies. The dispersion data considered in this paper were derived from waveforms generated using 2D finite-difference elastic wave-propagation simulation on models with and without subsurface anomalies, referred to as "treatment" and "control" models, respectively. In a previously published study, the treatment and control models were com-pared exclusively based on differences between their experimental dispersion data to determine whether or not the anomaly could likely be detected. This study examines whether those models previously categorized as containing a detectable anomaly based on their experimental dispersion data can be inverted to accurately resolve the anomaly's size, stiffness, and depth. In particular we focus on the effect of: (1) increasing anomaly lateral extent, and (2) increasing anomaly top depth on the resulting agreement between the 1D true solution Vs profiles (as defined at the center of the true model) and the inversion-derived Vs profiles from multiple parameterizations. The ability to resolve subsurface anomalies is shown to improve as the anomaly's lateral extent increases and as the anomaly moves closer to the ground surface. However, while the MASW method was able to reasonably recover the top depth and thickness of anomalies with large lateral extents (LE/AL > ~ 0.5), it was unable to accurately recover their velocity. In addition, as models with sufficient lateral extent were moved deeper into the model, MASW loses even its ability to accurately recover the anomaly's top depth and thickness. This is despite the fact that the anomalies presented were relatively thick (> 2 m) and with a significant impedance contrast (> 2) to the surrounding medium.

3.8 ACKNOWLEDGEMENTS

All inversions were performed using the DesignSafe-CI (Rathje et al., 2017) application SWbatch (Vantassel et al., 2020). To handle the large amount of results produced through the course of this study, SWprepost (Vantassel, 2020), an open-source Python package, was used for all surface-wave inversion pre- and post-processing. Author U.A. would like to thank the General Directorate of State Hydraulic Works (DSI) and the Republic of Turkey for supporting him in this research. Additionally, this material is based upon work supported by the National Science Foundation (NSF) Graduate Research Fellowship Program under Grant No. DGE – 1610403 and NSF Grant CMMI-1931162. Any opinions, findings, and conclusions or recommendations expressed in this material are those of the authors and do not necessarily reflect the views of NSF.

Chapter 4: Conclusions and Recommendations

This study examines the abilities and limitations of the MASW method to both detect and resolve subsurface anomalies. To address the limited literature available regarding the quantitative ability of the MASW method to detect subsurface anomalies, typical testing procedures were simulated using synthetic control (i.e., without an anomaly) and treatment (i.e., with an anomaly) models. The misfit between the dispersion data of the control and treatment models were summarized quantitatively and used to illustrate whether a particular anomaly could or could not likely be detected. To allow for practical usage of this study, the quantitative misfit values were used to create example feasibility plots such that the likelihood of detecting an anomaly of a given impedance contrast and geometry can be assessed prior to performing the field acquisition.

In short, results from this study reveal that the ability to detect an anomaly is largely dependent on its impedance contrast with the surrounding material and on its size/depth. Furthermore, a site with higher background velocities leads to greater chances for detection of anomalies at depth compared to a site containing soils with low velocities due to an increase in the measured wavelengths, provided the frequency range measured at both sites is consistent. For impedance contrasts greater than 1.0, an anomaly must be roughly half the length of the array used during testing to likely be detected, whereas at an impedance contrast less than 1.0, the anomaly may be as small as a quarter of the array length. As expected, the results show that as the thickness of an anomaly increases, the potential to detect it increases, while an increase in depth to the top of the same anomaly results in a decrease in its detectability. It should be noted again that while a misfit of 1.0 was used as a general guideline for the boundary of easy/likely detection in this study, misfits below 1.0 do not strictly indicate that an anomaly will not be detected; rather, a misfit below 1.0

indicates that these anomalies will be more difficult, or in general less likely, to be detected given typical levels of experimental dispersion data uncertainty.

While the first part of this study emphasized the importance of detecting anomalies when performing site characterization, the ability to accurately resolve irregular velocity profiles through inversion is a separate and more difficult matter. Detecting an anomaly is present does not necessarily mean that the anomaly may be resolved in terms of its shape and velocity. As such, the second part of this study examined the ability of the MASW method to accurately recover the size, stiffness, and depth of subsurface anomalies. In particular, investigations were conducted to examine the effects of: (1) increasing anomaly lateral extent, and (2) increasing anomaly top depth on the resulting agreement between the 1D true solution Vs profiles (as defined at the center of the true model) and the inversion-derived Vs profiles from multiple parameterizations. While the MASW method was able to reasonably recover the top depth and thickness of anomalies with large lateral extents (LE/AL > ~ 0.5), it was unable to accurately recover their velocity. In addition, as models with sufficient lateral extent were moved deeper into the model, MASW loses even its ability to accurately recover the anomaly's top depth and thickness. This is despite the fact that the anomalies presented were relatively thick (> 2 m) and with a significant impedance contrast (> 2) to the surrounding medium.

Appendix A: Additional Summary Plots of Relative Misfit and Inversion Results

This appendix contains some additional summary plots of relative misfit and inversion results that could not be included in the conference paper presented in Chapter 3.

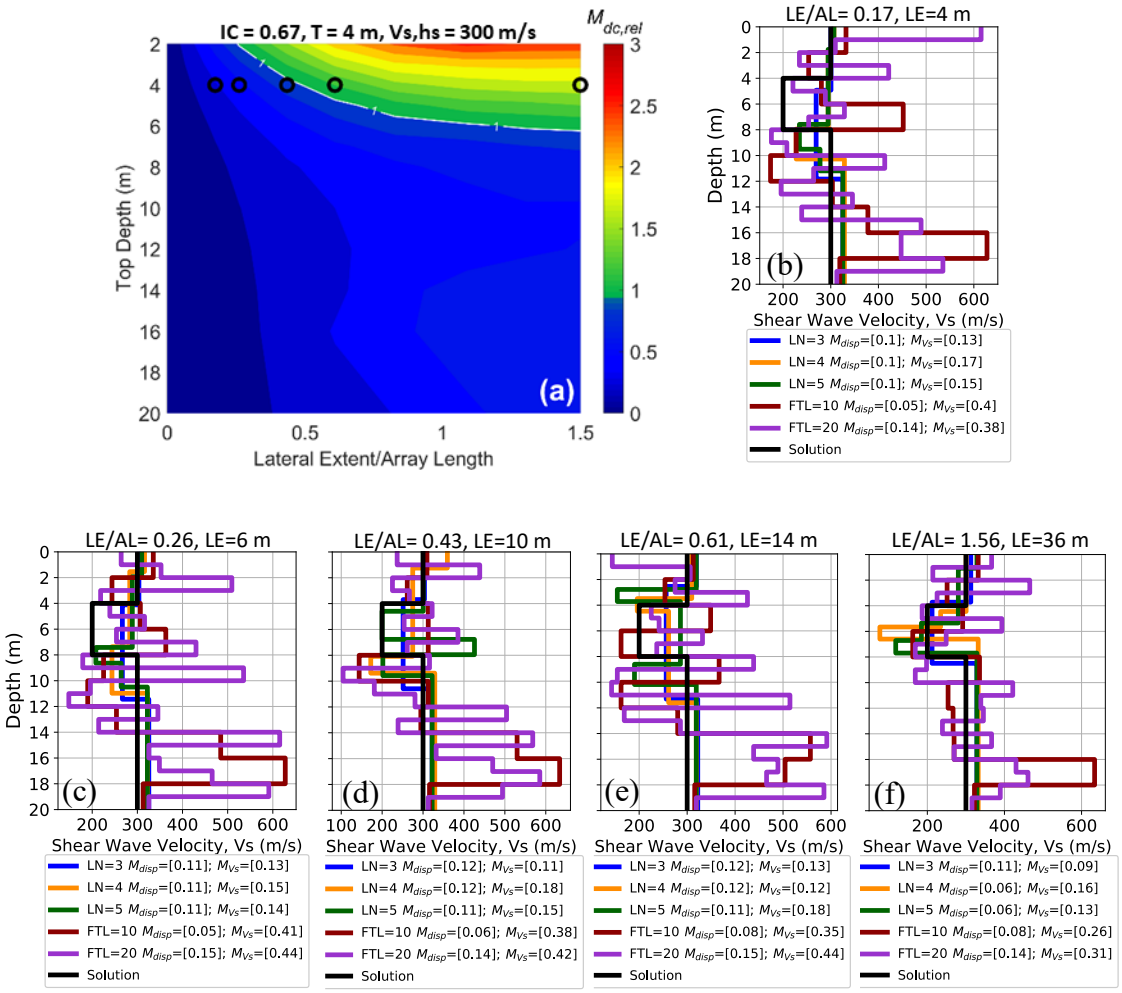

Figure A.1: Summary plot of misfit values for an impedance contrast of 0.67, half-space Vs of 300 m/s, thickness of 4, and top depth of 4 m (I0.67-H300-T4-D4). In this example, the top depth and thickness of each anomaly is the same while the lateral extent changes for each anomaly. The lateral extent/array length ratio of the anomalies whose Vs profiles (b-f) are shown above are 0.17, 0.26, 0.43, 0.61, and 1.56 m, respectively.

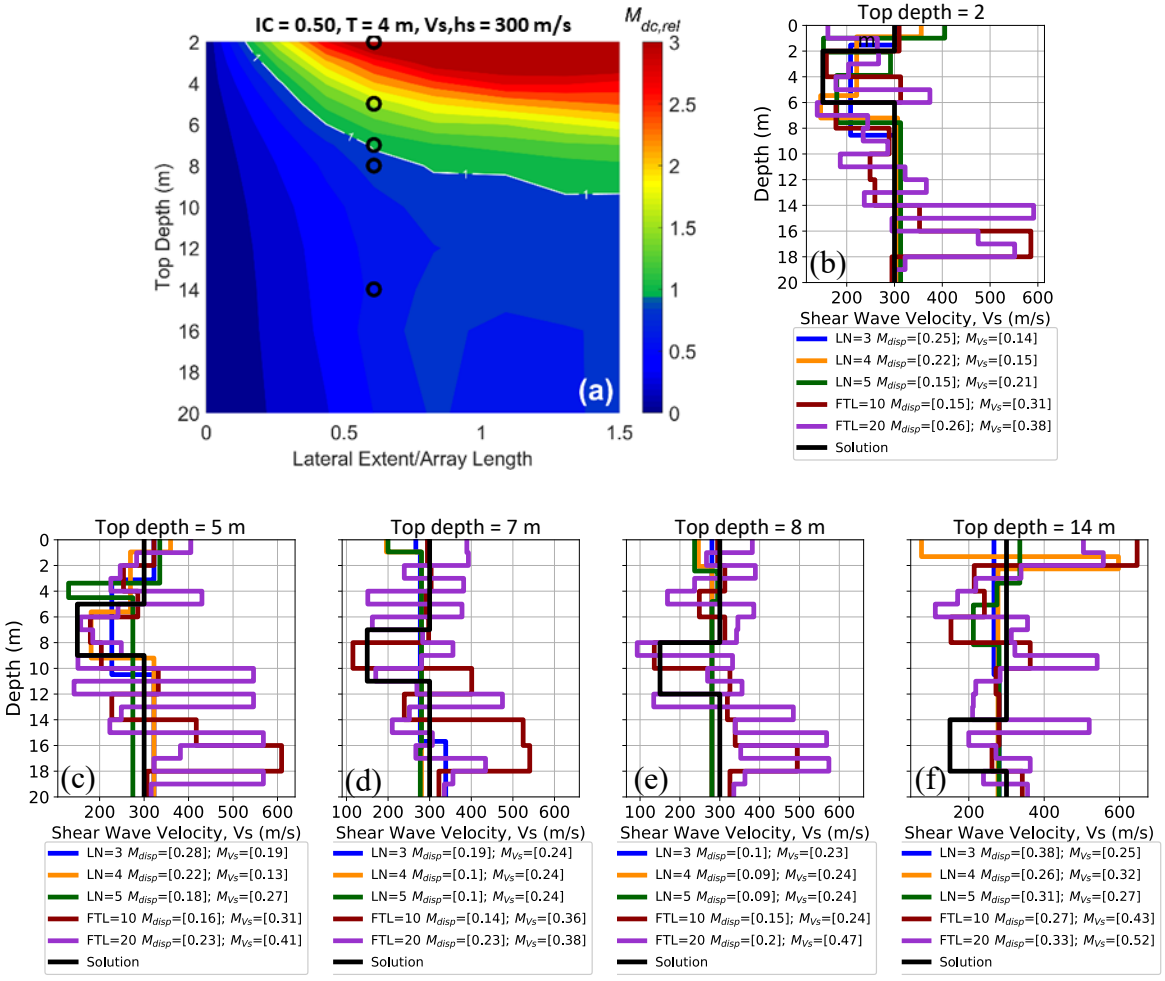

Figure A.2: Summary plot of misfit values for an impedance contrast of 0.5, half-space Vs of 300 m/s, thickness of 4, and lateral extent of 14 m (I0.5-H300-T4-L14). In this example, lateral extent and the thickness of each anomaly is the same while the top depth changes for each anomaly. Top depth of the anomalies whose Vs profiles (b-f) are shown above are 2, 5, 7, 8 and 14 m, respectively.

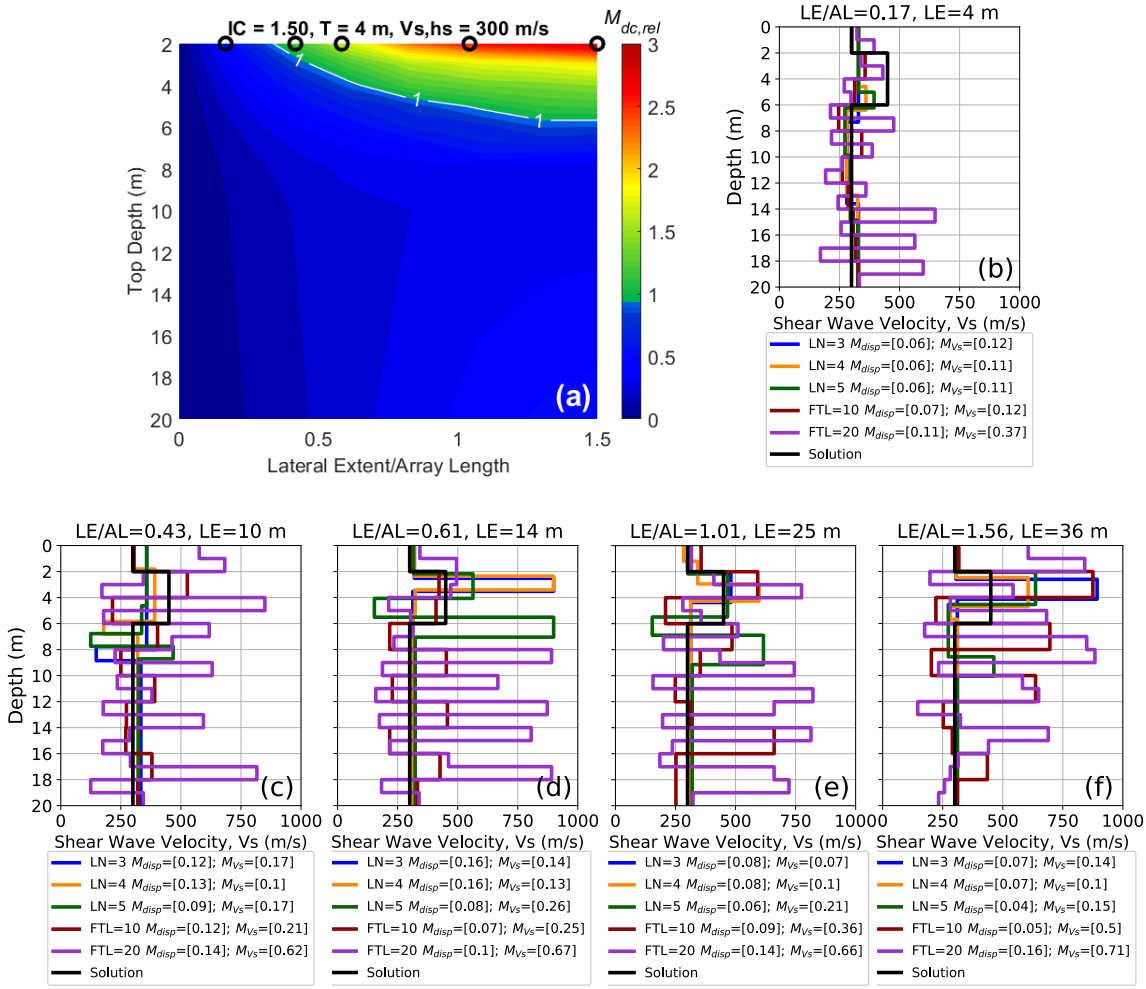

Figure A.3: Summary plot of misfit values for an impedance contrast of 1.5, half-space Vs of 300 m/s, thickness of 4, and top depth of 2 m (I1.5-H300-T4-D2). In this example, the top depth and thickness of each anomaly is the same while the lateral extent changes for each anomaly. The lateral extent/array length ratio of the anomalies whose Vs profiles (b-f) are shown above are 0.17, 0.43, 0.61, 1.01, and 1.56 m, respectively.

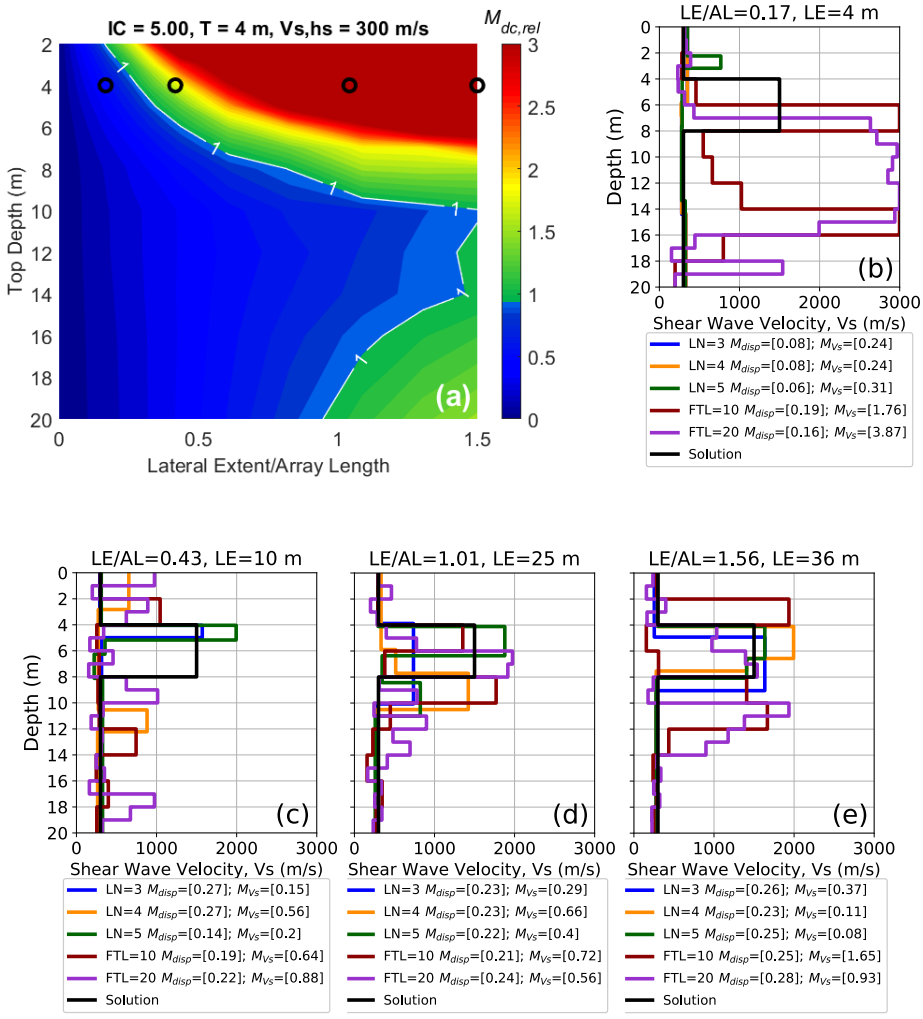

Figure A.3: Summary plot of misfit values for an impedance contrast of 5, half-space Vs of 300 m/s, thickness of 4, and top depth of 4 m (I5-H300-T4-D4). In this example, the top depth and thickness of each anomaly is the same while the lateral extent changes for each anomaly. The lateral extent/array length ratio of the anomalies whose Vs profiles (b-f) are shown above are 0.17, 0.43, 1.01, and 1.56 m, respectively.

References

Brossier, Romain, Stéphane Operto, and Jean Virieux. 2010. “Which Data Residual Norm for Robust Elastic Frequency-Domain Full Waveform Inversion?” *Geophysics* 75 (3). https://doi.org/10.1190/1.3379323.

Chambers, Jonathan E., Oliver Kuras, Philip I. Meldrum, Richard D. Ogilvy, and Jonathan Hollands. 2006. “Electrical Resistivity Tomography Applied to Geologic, Hydrogeologic, and Engineering Investigations at a Former Waste-Disposal Site.” *Geophysics* 71 (6). https://doi.org/10.1190/1.2360184.

Cox, B. R., and C. M. Wood. 2011. “Surface Wave Benchmarking Exercise: Methodologies, Results and Uncertainties.” *GeoRisk 2011*, no. 122 m: 403–10.

Cox, B. R., C. M. Wood, and D. P. Teague. 2014. “Synthesis of the UTexas1 Surface Wave Dataset Blind-Analysis Study: Inter-Analyst Dispersion and Shear Wave Velocity Uncertainty,” 850–59. https://doi.org/10.1061/9780784413272.083.

Cox, Brady R., and David P. Teague. 2016. “Layering Ratios: A Systematic Approach to the Inversion of Surface Wave Data in the Absence of a Priori Information.” *Geophysical Journal International* 207 (1): 422–38. https://doi.org/10.1093/gji/ggw282.

Debeglia, Nicole, Adnand Bitri, and Pierre Thierry. 2006. “Karst Investigations Using Microgravity and MASW; Application to Orléans, France.” *Near Surface Geophysics* 4 (4): 215–25. https://doi.org/10.3997/1873-0604.2005046.

Foti, S. 2000. “Multistation Methods for Geotechnical Characterization Using Surface Waves.” *Politecnico Di Torino Ph D Dissertation* 42: 315–23. https://doi.org/10.1590/S0036-36342000000400006.

Foti, S., Fabrice. Hollender, Flora. Garofalo, Dario. Albarello, Michael. Asten, Pierre Yves. Bard, Cesare. Comina, et al. 2018. *Guidelines for the Good Practice of Surface Wave Analysis: A Product of the InterPACIFIC Project*. *Bulletin of Earthquake Engineering*. Vol. 16. https://doi.org/10.1007/s10518-017-0206-7.

Garofalo, F., S. Foti, F. Hollender, P. Y. Bard, C. Cornou, B. R. Cox, M. Ohrnberger, et al. 2016. “InterPACIFIC Project: Comparison of Invasive and Non-Invasive Methods for Seismic Site Characterization. Part I: Intra-Comparison of Surface Wave Methods.” *Soil Dynamics and Earthquake Engineering* 82: 222–40. https://doi.org/10.1016/j.soildyn.2015.12.010.

Giulio, Giuseppe Di, Alexandros Savvaidis, Matthias Ohrnberger, Marc Wathelet, Cecile Cornou, Brigitte Knapmeyer-Endrun, Florence Renalier, Nikos Theodoulidis, and Pierre Yves Bard. 2012. “Exploring the Model Space and Ranking a Best Class of Models in Surface-Wave Dispersion Inversion: Application at European Strong-Motion Sites.” *Geophysics* 77 (3). https://doi.org/10.1190/geo2011-0116.1.

Groves, Paul, Giovanni Cascante, Dave Dundas, and P. K. Chatterji. 2011. “Use of Geophysical Methods for Soil Profile Evaluation.” *Canadian Geotechnical Journal* 48 (9): 1364–77. https://doi.org/10.1139/t11-044.

Haskell, By N A. 1953. “The Dispersion of Surface Waves on Multilayered Media.” 43 (1): 17–34.

Hirsch, Markus, Laurence R. Bentley, and Peter Dietrich. 2008. “A Comparison of Electrical Resistivity, Ground Penetrating Radar and Seismic Refraction Results at a River Terrace Site.” *Journal of Environmental and Engineering Geophysics* 13 (4): 325–33. https://doi.org/10.2113/JEEG13.4.325.

Hock, Silke, Julian Ivanov, and Richard D. Miller. 2007. “Test for Detecting an Impermeable Water Barrier in an Earth-Fill Dam in Austria Using MASW Method.” *Proceedings of the Symposium on the Application of Geophyics to Engineering and Environmental Problems, SAGEEP* 1: 610–17. https://doi.org/10.4133/1.2924720.

Ismail, Ahmed, F. Brett Denny, and Mohamed Metwaly. 2014. “Comparing Continuous Profiles from MASW and Shear-Wave Reflection Seismic Methods.” *Journal of Applied Geophysics* 105: 67–77. https://doi.org/10.1016/j.jappgeo.2014.03.007.

Ivanov, Julian, Richard D. Miller, Pierre Lacombe, Carole D. Johnson, and John W. Lane. 2006. “Delineating a Shallow Fault Zone and Dipping Bed Rock Strata Using Multichannal Analysis of Surface Waves with a Land Streamer.” *Geophysics* 71 (5). https://doi.org/10.1190/1.2227521.

Ivanov, Julian, Richard D Miller, Shelby L Peterie, and Kansas Geological Survey. 2016. “Detecting and Delineating Voids and Mines Using Surface Wave Methods in Galena , Kansas,” 2344–50.

Ivanov, Julian, Kansas Geological Survey, Carole D Johnson, John W Lane, U S Geological Survey, Richard D Miller, Drew Clemens, and U S Army Corps. 2009. “Near-Surface Evaluation of Ball Mountain Dam , Vermont , Using Multi-Channel Analysis of Surface Waves (MASW) and Refraction Tomography Seismic Methods on Land-Streamer Data SEG Houston 2009 International Exposition and Annual Meeting Ball Mntn Dam Eval.” *Access*, 1454–58.

Ivanov, Julian, Kansas Geological Survey, and Richard D Miller. 2008. “SOME PRACTICAL ASPECTS OF MASW ANALYSIS AND PROCESSING,” 1186–98.

Köhn, D., D. De Nil, A. Kurzmann, A. Przebindowska, and T. Bohlen. 2012. “On the Influence of Model Parametrization in Elastic Full Waveform Tomography.” *Geophysical Journal International* 191 (1): 325–45. https://doi.org/10.1111/j.1365-246X.2012.05633.x.

Mahvelati, Siavash, and Joseph Thomas Coe. 2017. “The Use of Two Dimensional (2D) Multichannel Analysis of Surface Waves (MASW) Testing to Evaluate the Geometry of an Unknown Bridge Foundation.” *Geotechnical Special Publication* 2012 (GSP 277): 657–66. https://doi.org/10.1061/9780784480441.069.

Mirzanejad, Majid, and Khiem T. Tran. 2019. “3D Viscoelastic Full Waveform Inversion of Seismic Waves for Geotechnical Site Investigation.” *Soil Dynamics and Earthquake Engineering* 122 (October 2018): 67–78. https://doi.org/10.1016/j.soildyn.2019.04.005.

Mohamed, Adel M.E., A.S.A. Abu El Ata, F. Abdel Azim, and M.A. Taha. 2013. “Site-Specific Shear Wave Velocity Investigation for Geotechnical Engineering Applications Using Seismic Refraction and 2D Multi-Channel Analysis of Surface Waves.” *NRIAG Journal of Astronomy and Geophysics* 2 (1): 88–101. https://doi.org/10.1016/j.nrjag.2013.06.012.

Nolan, Jeffery J, Steven D Sloan, Seth W Broadfoot, Jason R Mckenna, and Owen M Metheny. 2011. “Near-Surface Void Identification Using MASW and Refraction Tomography Techniques. In SEG Technical Program Expanded Abstracts 2011 (Pp. 1401-1405). Society of Exploration Geophysicists.”

Nolet, Guust, and Giuliano F. Panza. 1976. “Array Analysis of Seismic Surface Waves: Limits and Possibilities.” *Pure and Applied Geophysics PAGEOPH* 114 (5): 775–90. https://doi.org/10.1007/BF00875787.

Pan, Yudi, Lingli Gao, and Thomas Bohlen. 2019. “High-Resolution Characterization of Near-Surface Structures by Surface-Wave Inversions: From Dispersion Curve to Full Waveform.” *Surveys in Geophysics* 40 (2): 167–95. https://doi.org/10.1007/s10712-019-09508-0.

Park, Choon B., Richard D. Miller, and Jianghai. Xia. 1999. “Multichannel Analysis of Surface Waves.” *Geophysics* 64 (3): 800–808. https://doi.org/https://doi.org/10.1190/1.1444590.

Park, Choon B. 2005. “Park, C. B. (2005). MASW Horizontal Resolution in 2D Shear-Velocity (Vs) Mapping. Open-File Report, Lawrence: Kansas Geologic Survey.”

Rahimi, Salman, Clinton M. Wood, Folaseye Coker, Timothy Moody, Michelle Bernhardt-Barry, and Behdad Mofarraj Kouchaki. 2018. “The Combined Use of MASW and Resistivity Surveys for Levee Assessment: A Case Study of the Melvin Price Reach of the Wood River Levee.” *Engineering Geology* 241 (April): 11–24. https://doi.org/10.1016/j.enggeo.2018.05.009.

Rathje, Ellen M., Clint Dawson, Jamie E. Padgett, Jean Paul Pinelli, Dan Stanzione, Ashley Adair, Pedro Arduino, et al. 2017. “DesignSafe: New Cyberinfrastructure for Natural Hazards Engineering.” *Natural Hazards Review* 18 (3): 1–7. https://doi.org/10.1061/(ASCE)NH.1527-6996.0000246.

Sambridge, Malcolm. 1999. “Geophysical Inversion with a Neighbourhood Algorithm — I . Searching a Parameter Space,” 479–94.

Shakir, Ammar M., Sebastiano Foti, Flora Garofalo, Basim R. Hijab, and Amer A. Laftah. 2013. “Laterally Constrained Inversion of Surface Wave Data at Najaf City (Iraq).” *Soil Dynamics and Earthquake Engineering* 45: 89–95. https://doi.org/10.1016/j.soildyn.2012.11.003.

Sloan*, Steven D., J. Tyler Schwenk, Robert H. Stevens, and Benjamin W. Butler. 2015. “Hazard Assessment and Site Characterization at an Oil and Gas Well Site Using Surface Wave Methods,” 114–17. https://doi.org/10.1190/iceg2015-032.

Sloan, Steven D., Jeffery J. Nolan, Seth W. Broadfoot, Jason R. McKenna, and Owen M. Metheny. 2013. “Using Near-Surface Seismic Refraction Tomography and Multichannel Analysis of Surface Waves to Detect Shallow Tunnels: A Feasibility Study.” *Journal of Applied Geophysics* 99: 60–65. https://doi.org/10.1016/j.jappgeo.2013.10.004.

Stokoe, Kenneth H., Brady R. Cox, Yin Cheng Lin, Min Jae Jung, Farn Yuh Menq, James A. Bay, Brent Rosenblad, and Ivan Wong. 2006. “Use of Intermediate to Large Vibrators as Surface Wave Sources to Evaluate Vs Profiles for Earthquake Studies.” *19th Symposium on the Application of Geophysics to Engineering and*

Environmental Problems, SAGEEP 2006: Geophysical Applications for Environmental and Engineering Hazzards - Advances and Constraints 2: 1241–58. https://doi.org/10.4133/1.2923582.

Suto, Koya, Terra Australis Geophysica, and Ross Kristinof. 2014. "AN MASW SURVEY TO ASSESS FLOOD DAMAGED ROAD – A CASE HISTORY USE OF AN MASW SURVEY TO ASSESS FLOOD DAMAGED ROAD – A CASE HISTORY," no. March 2014. https://doi.org/10.1190/SAGEEP.27-143.

Thomson, William T. 1950. "Transmission of Elastic Waves through a Stratified Solid Medium." *Journal of Applied Physics* 21 (2): 89–93. https://doi.org/10.1063/1.1699629.

Vantassel, J. P. (2020) jpvantassel/swprepost: latest (Concept). doi: 10.5281/zenodo.3839998.

Vantassel, J. P., Gurram, H. and Cox, B. R. (2020) jpvantassel/swbatch: latest (Concept). doi: 10.5281/zenodo.3840546.

Vantassel, Joseph P., and Brady R. Cox. 2020. "SWinvert: A Workflow for Performing Rigorous Surface Wave Inversions," 1–25. http://arxiv.org/abs/2005.11820.

Wathelet, M., D. Jongmans, and M. Ohrnberger. 2004. "Surface-Wave Inversion Using a Direct Search Algorithm and Its Application to Ambient Vibration Measurements." *Near Surface Geophysics* 2 (4): 211–21. https://doi.org/10.3997/1873-0604.2004018.

Wathelet, Marc, Jean Luc Chatelain, Cécile Cornou, Giuseppe Di Giulio, Bertrand Guillier, Matthias Ohrnberger, and Alexandros Savvaidis. 2020. "Geopsy: A User-Friendly Open-Source Tool Set for Ambient Vibration Processing." *Seismological Research Letters* 91 (3): 1878–89. https://doi.org/10.1785/0220190360.

Xia, J., Recep Cakir, Richard D. Miller, Chong Zeng, and Yinhe Luo. 1999. "Estimation of Near-Surface Shear-Wave Velocity by Inversion of Love Waves." *79th Society of Exploration Geophysicists International Exposition and Annual Meeting 2009, SEG 2009* 64 (3): 1390–95.

Xia, J., C. Chen, P. H. Li, and M. J. Lewis. 2004. "Delineation of a Collapse Feature in a Noisy Environment Using a Multichannel Surface Wave Technique." *Geotechnique* 54 (1): 17–27. https://doi.org/10.1680/geot.2004.54.1.17.

Xia, Jianghai, Richard D. Miller, Choon B. Park, James A. Hunter, and James B. Harris. 2000. "Comparing Shear-Wave Velocity Profiles from MASW with Borehole Measurements in Unconsolidated Sediments, Fraser River Delta, B.C., Canada." *Journal of Environmental and Engineering Geophysics* 5 (3): 1–13. https://doi.org/10.4133/jeeg5.3.1.

Zywicki, D. J. "Advanced Signal Processing Methods Applied to Engineering Analysis of Seismic Surface Waves", Georgia Insti-tute of Technology, 1999.

Vita

Ugur Arslan was born in Sanliurfa, Turkey, and moved to the capital, Ankara, in 2000. He graduated from Dikmen Anatolian High School in Ankara in 2011 and started his undergraduate at Gazi University in Fall 2012. He graduated in Civil Engineering at Gazi University in June 2016. After working as a civil and geotechnical engineer for about a year, he started his graduate education in Geotechnical Engineering at the University of Texas at Austin in Spring 2019.

Email: 1205ugur@gmail.com

This thesis was typed by the author